Volume 43 | Number 5 | 7 March 2014 | Pages 1341–1790

Chem Soc Rev

Chemical Society Reviews

www.rsc.org/chemsocrev

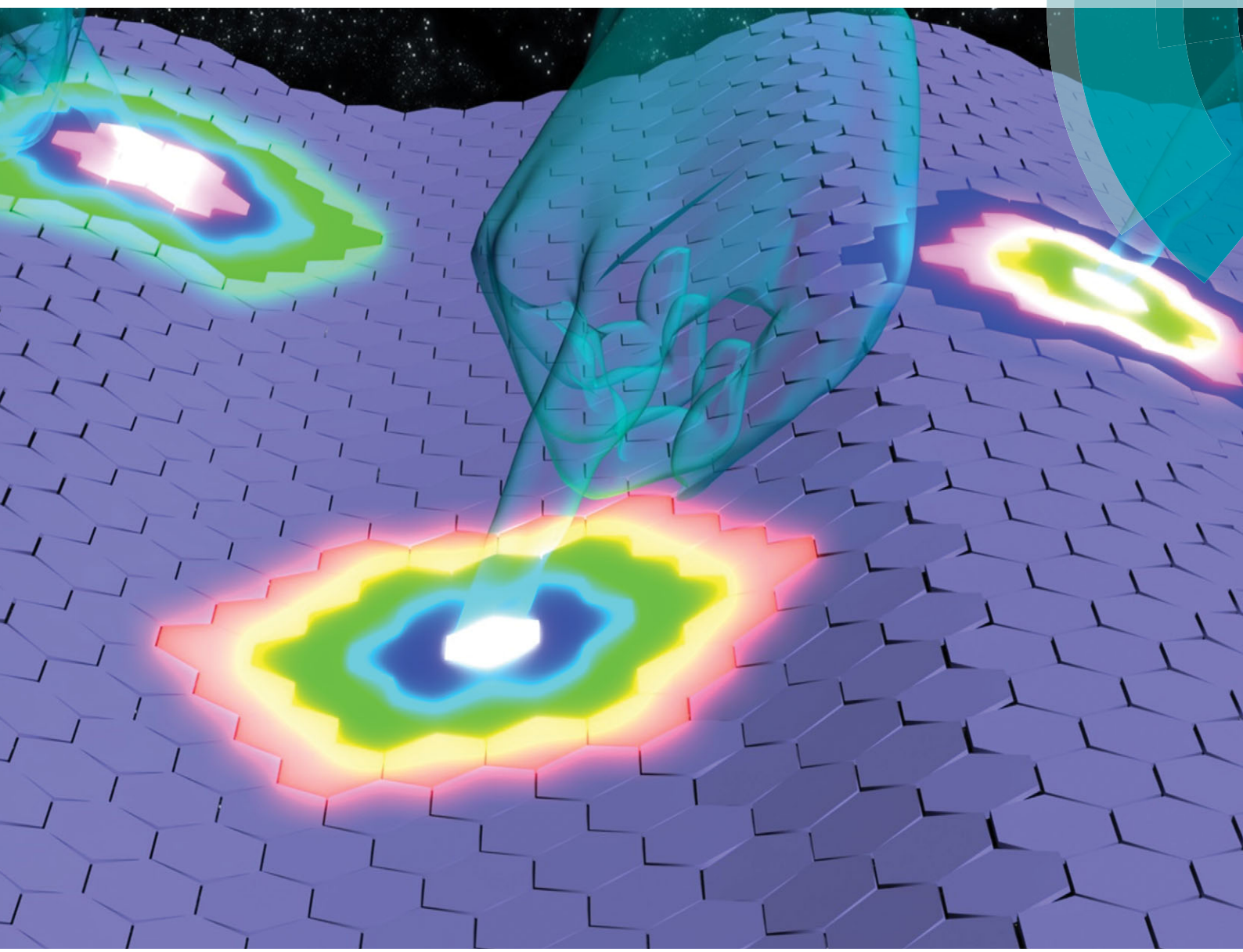

ISSN 0306-0012

ROYAL SOCIETY OF CHEMISTRY

REVIEW ARTICLE

Xi Wang, Wei Tian, Meiyong Liao, Yoshio Bando and Dmitri Golberg
Recent advances in solution-processed inorganic nanofilm photodetectors

Chem Soc Rev

REVIEW ARTICLE

View Article Online
View Journal | View Issue

Cite this: *Chem. Soc. Rev.*, 2014, **43**, 1400

Recent advances in solution-processed inorganic nanofilm photodetectors

Xi Wang,*† Wei Tian,*† Meiyong Liao, Yoshio Bando and Dmitri Golberg*

Received 1st October 2013

DOI: 10.1039/c3cs60348b

www.rsc.org/csr

As important opto-electronical devices, nanofilm photodetectors constructed from inorganic low-dimensional nanostructures have drawn prime attention due to their significance in basic scientific research and potential technological applications. This review highlights a selection of important topics pertinent to inorganic nanofilm photodetectors processed *via* solution strategies. This article begins with a description of the advantages and drawbacks of nanofilm-based photodetectors *versus* 1D nanostructure-based ones, and then introduces rational design and controlled syntheses of various nanofilms *via* different wet-chemical routes, and then mainly focuses on their optoelectronic properties and applications in photodetectors based on the different types of nanofilms. Finally, the general challenges and the potential future directions of this exciting research and technology area are presented.

1. Introduction

Photodetectors built from inorganic low-dimensional nanostructures such as 1D nanowires and 2D nanofilms have attracted extensive attention from scientists due to their significance in basic scientific research and optoelectronic applications. Research on high-performance photodetectors is beyond doubt one of the hottest fields in modern nanoscience and nanotechnology. Based on data from the Institute of Scientific Information (ISI), since 2000 the number of publications related to photodetector-related topics has exceeded 13 000. Over the past ten years, individual 1D nanostructure-based photodetectors have been a pursued research topic due to their high quantum-efficiency, but the common top-down approach usually requires a complex and costly lithography process including organic film coating, exposure, metal evaporation and lift-off. Technologically, if the nanostructures could be assembled in a thin-film form, the metal electrodes can be easily deposited on such films

World Premier International Center for Materials Nanoarchitectonics (WPI-MANA), International Center for Young Scientists (ICYS), National Institute for Materials Science (NIMS), Namiki 1-1, Tsukuba, Ibaraki, 305-0044, Japan.
E-mail: WANG.Xi2@nims.go.jp, WEI.Tian@nims.go.jp, GOLBERG.Dmitri@nims.go.jp
† These authors contributed equally.

Xi Wang

Xi Wang received his PhD degree in Physical Chemistry from the Institute of Chemistry, Chinese Academy of Sciences (ICCAS) under the supervision of Prof. Jiannian Yao in 2010. Afterwards he joined the National Institute for Materials Science (NIMS) as a JSPS postdoctoral fellow of Prof. Yoshio Bando's group and then became a fellow of the International Center for Young Scientists (ICYS) within NIMS. His research interests include the controlled synthesis and exploration of fundamental physical properties of inorganic functional nanomaterials, as well as their promising applications in energy science, electronics and optoelectronics.

Wei Tian

Wei Tian received his BS degree in Materials Science from Chang'an University in 2008, and then received his Master's degree from Zhejiang University in 2011. Afterwards he joined the National Institute for Materials Science (NIMS) to pursue his PhD degree as a NIMS junior researcher, under the supervision of Prof. Yoshio Bando. His research interests include the controlled fabrication and characterization of 1D nanostructures and their device application in electronics and optoelectronics.

using a hand-operable metal microwire as a mask, and also the performances of thin film photodetectors may further be optimized after the integration of a large number of individual nanostructures. Therefore, very recently the research on inorganic nanofilms using a wet-chemical bottom-up approach has received worldwide attention from nanoscience and nanotechnology experts; this has led to a notable increase in the number of related research papers and patents. A variety of nanofilm-based photodetectors, such as ZnO,[1,2] ZnS,[1] SnO_2,[3] $NiCo_2O_4$,[4] CdS,[5] Bi_2S_3,[6–8] Zn_2GeO_4,[9] P3HT:CdSe,[10] Cu_2O,[11] In_2S_3,[12] and In_2O_3,[13] have been prepared by using solution-processed routes. In the past years, our group performed an in-depth study related to this field and constructed several new kinds of photodetectors made of various nanostructures,[14–43] *e.g.* pure nanomaterials and/or doped- and hereto-nanostructures. Up to now, there have been many original and review articles devoted to nanostructured materials and set-ups used in photodetectors, these include quantum-dots,[44–47] quantum-well,[48–51] 1D nanostructures,[52–55] Ge-on-Si,[56] ZnO,[57] organic thin-film,[58] Si,[59] lnP,[60] wide-bandgap semiconductors for ultraviolet light detection,[61] gaseous[62] and other kinds.[63–67] However, there have been a very few comprehensive reviews focusing on a variety of solution-processed techniques used for inorganic nanofilm photodetector fabrication. This critical review highlights a selection of important topics pertinent to this field over the last 5 years. The aim of this review is to meet the growing demands of the related technologies.

Clearly, solution-processed nanofilm photodetectors show obvious merits over the conventional crystalline semiconductor devices.[42,43] Importantly, their performances may significantly be improved due to photocurrents collected from a large number of building blocks, as compared with the individual nanostructure-based photodetectors. Therefore, some main issues for applications may effectively be tackled, *e.g.* scale-up production, stability, and reproducibility. Flexible, fully transparent and high-performance ultrathin film photodetectors can be produced. In this review, we attempt to provide the readers with an essential introduction to this fast-growing field. We begin with an introduction to the work principle of a photodetector, followed by a detailed discussion on the advantages and disadvantages of the nanofilm photodetectors *versus* 1D nanostructure-based ones. Then we highlight the recent advances in synthetic strategies for various building blocks along with the assembly and

Meiyong Liao

Meiyong Liao received his Bachelor's and Master's degrees from Lanzhou University in 1996 and 1999, respectively, and his PhD degree from the Institute of Semiconductors, Chinese Academy of Sciences in 2002. From 2002 to 2004, he was a visiting Associate Professor in Kyoto University. He joined the National Institute for Materials Science, Japan, and worked as a postdoctoral researcher during 2004–2008. In April 2008, he was promoted as a Senior Researcher at NIMS. His current research fields are semiconductor electronic and photonic devices, and MEMS/NEMS.

Yoshio Bando

Yoshio Bando received his PhD degree from Osaka University in 1975 and joined the National Institute for Research in Inorganic Materials (at present NIMS) in the same year. From 1979 to 1981 he worked as a visiting researcher at Arizona State University. Currently, he is a Chief Operating Officer (COO) of the International Center for Materials Nanoarchitectonics (MANA) and a Fellow within the National Institute for Materials Science (NIMS). He is also a visiting Professor at both Waseda University and the University of Tokyo. His current research concentrates on the synthesis and properties of various inorganic nanostructures and their TEM characterizations. The H-index of his publications is 81. He also holds more than 150 patents. He received the 16th Tsukuba Prize in 2005 for his studies on novel inorganic nanotubes and nanothermometers and the 2012 Thomson Reuters Research Front Award for his investigations on 1D-nanostructures.

Dmitri Golberg

Dmitri Golberg obtained his PhD degree from the Central Research Institute for Ferrous Metallurgy, Moscow, Russia, in 1990, and joined the National Institute for Materials Science (NIMS), Tsukuba, Japan, five years later. To date, he has authored and co-authored more than 500 original papers and more than 100 patents. The H-index of his publications is 67. In 2005 he was awarded the 16th Tsukuba Prize for his studies on inorganic nanotubes using electron microscopy, and in 2012 he became a recipient of the 3rd Thomson Reuters Research Front Award for his studies on 1D-nanomaterials. He is currently a Unit Director and a Principal Investigator within the WPI International Center for Materials Nanoarchitectonics (MANA) of NIMS, and a Professor of the University of Tsukuba. His current research focuses on nanoscale material synthesis and their electrical, mechanical, thermal and optical properties studied in a transmission electron microscope.

transfer techniques of the 2D crystals into integrated films. We further present some progress in the construction of nanofilm-based photodetectors. The key points of each step: *e.g.* preparation, structure modulation, assembly and transfer processes, device construction, and performance optimization are also presented. We conclude this review with critical comments on the advantages and experimental challenges, as well as some perspectives for the future research and development in this field.

2. Advantages and disadvantages of nanofilm photodetectors *vs.* 1D nanostructure-based ones

A photoconductor, consisting of a semiconductor with the two Ohmic contacts, is essentially a radiation-sensitive resistor.[68] When a photon with energy larger than the band-gap energy of the semiconductor is absorbed, an electron–hole pair is produced, thereby changing the electrical conductivity of the material. There are two main mechanisms to evidence a photoresponse in an inorganic semiconductor. One is a fast band-to-band recombination in the bulk, with time characteristics in the nanosecond range. The second one is a hole-trapping mechanism based on the existence of chemisorbed oxygen molecules at the surfaces. The latter is currently considered to be dominant for nanoscale materials.[69] The schematic structure and operation of a one-dimensional (1D) nanostructures based photodetector and a nanofilm photoconductor are shown in Scheme 1.

Recently, 1D nanostructures have been widely used for constructing high-performance photodetectors. The large surface-to-volume ratio and the presence of deep level surface trap states in nanowires greatly prolongs the photocarrier lifetime; the reduced dimensionality of the active area in nanowire devices shortens the carrier transit time. Indeed, the combination of a long lifetime and short transit time of charge carriers can result in substantial photoconductive gain.[70,71] However, all individual nanostructure based devices are fabricated by a microfabrication process using a combination of lithography, etching and deposition. This process is complicated, time-consuming and uneconomic, thus hampering the development of reliable practical routes. Moreover, the performance of devices critically depends on the quality of the Ohmic contacts between a nanostructure and the electrodes, so that the construction of reproducible and stable contacts is also hard. In addition, typically 1D nanostructures dispersed on an insulating substrate are randomly selected to fabricate individual nanostructure-based devices. The uniformity of nanostructures in composition and shape does not guarantee their uniformity in optoelectronic properties and photodetector performance. Therefore, the stability and reproducibility of individual nanostructure-based device performance are far from perfect. Solution-processed nanofilm devices have some advantages over conventional crystalline semiconductor devices and individual nanostructure-based ones in terms of ease in fabrication, large device area, physical flexibility, and most importantly, low cost. Also, a photocurrent coming out of the nanofilm based device is collected from a large number of simultaneously operating nanostructures rather than from a single one, leading to a significant current enhancement.

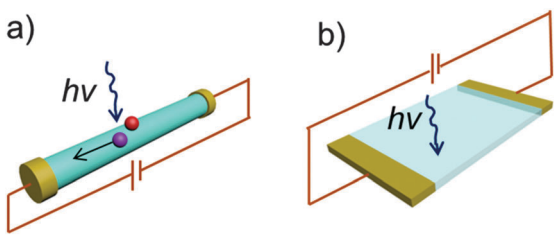

Scheme 1 (a) The schematic structure and operation of a one-dimensional (1D) nanostructures-based photodetector, and (b) a nanofilm photoconductor.

3. Solution-based routes for nanofilm assembly

Solution-based self-assembly, as a bottom-up approach that can be used under mild conditions, has high technical attractiveness for rational design and construction of nanoarchitectures as device components because of methodological simplicity, low cost, and low environmental impact.[72,73] Recently, few-layered films of spherical or polyhedral nanoparticles with high regularity were produced by some solution-based techniques, *e.g.* spin-coating, electrospinning, the Langmuir–Blodgett (LB) method[73] and oil/water interfacial self-assembly.[74,75] In contrast to nanoparticles, platelet crystallites, because of their peculiar two-dimensional (2D) anisotropy, may be naturally and easily tiled up to form a film.[77–86] Self-assembly of 2D crystallites, partly inspired by the ordered aragonite platelets in the nacreous layers of mollusk shells,[76,77] has received intensive attention from the viewpoint of hybrid or reinforced nanocomposites, photonic and liquid crystallite applications, as well as for luminescent films, *etc.*[80–86] In spite of the fact that it is relatively easy to align the platelets parallel to the substrate surface, in-plane azimuth orientation is usually random and the regularity is typically low.[78,85] This is caused by the non-uniform geometric shape and broad size distribution of 2D crystallites. The cavity gaps among neighbouring crystallites and low regularity hinder the uses of resulting films for high-end devices.

3.1 Spin-coating

Spin-coating is an out-of-equilibrium technique for quick and reproducible production of films made of colloidal crystals. In this part, we present a short overview of the recent progress with regards to theoretical and experimental studies of the spin coating of colloidal particles into a nanofilm. We also discuss some nanofilms with partially ordered structures obtained by applying electric or magnetic fields during the spin-coating procedure.

Spin coating is a widespread practice in modern science and engineering. By using this method, uniform coatings of inorganic–organic materials can be deposited on a flat surface.[87,88] In fact, spin coating has been widely used in the microelectronics industry. For example, a smooth, uniform photoresist film of predictable

and reproducible thickness on silicon wafers is highly needed at the initial stage of the lithographic patterning process.[89] Many efforts have been taken to catalogue the dependence of film uniformity on the experimental parameters during coating and using standard photoresists.[90–92] On the other hand, in order to better guide the practice, it is necessary to perform a theoretical study of spin-coating based on the principles of hydrodynamics. Although this system is rather complex with respect to physics and mathematics, some insight into the effectiveness and the limitations of the process may still be provided by tentative theoretical analysis.

In general, the spin-coating process consists of four steps: (a) dispensation, (b) acceleration, (c) flow dominated stage, (d) evaporation dominated stage. The properties of the coated films are affected by many factors such as final rotation speed, acceleration, and fume exhaust. Repeatability is regarded as one of the most important factors in spin-coating, as subtle variations in the parameters in a spin-coating process can lead to drastic variations in the quality of the coated film. In this respect, Bornside *et al.*[93] performed important work. They set the rate of evaporation (e) as:

$$e = k(x_A^0 - x_A^\infty)$$

Where k represents the mass transfer coefficient, x_A^0 is the initial concentration of solvent in the coating liquid, and x_A^∞ is the mass fraction of solvent in the coating liquid that would be in equilibrium with the mass fraction of solvent in the bulk gas. Therefore, the thickness can be decently expressed. It also suggests that the basic level of analysis is able to demonstrate how to produce a film of uniform thickness based only on the process parameters and material properties. In addition, theoretical studies are lingering far behind the experiments, thus a more complicated process needs to be considered, such as the effects of frontal propagation,[94] viscosity and diffusivity as a function of z.[95] These efforts should guide one to reliably fabricate high-quality nano-films by spin-coating.

A traditional film obtained by a spin-coating method usually has one kind of colloidal spheres with uniform size. Alternatively, self-organized nanofilms consisting of larger (L) and smaller (S) binary colloidal crystals, has drawn decent attention with respect to applications, such as 3D photonic crystals with full bandgaps.[97] Therefore, the diameter ratios of the smaller to larger sphere (γ) becomes highly important, that determines the phase behaviour in this binary sphere-constructed film. Especially, Wang and Möhwald[96] presented a stepwise spin-coating approach for constructing a film, in which the layers of larger and smaller spheres were formed consecutively. As shown in Fig. 1a, colloidal larger spheres were first placed on the substrate by spin-coating and a smaller-sphere layer was subsequently formed on them. The key point in this synthesis is that there exists two kinds of cavities in large spheres, including the intersites between the hexagonally close-packed large spheres and the recesses between them. They can serve as traps for placing small spheres. Therefore, the small spheres were first confined within the lower intersites, then within the recesses, and eventually a complete *hcp* monolayer of small colloidal spheres on top of the monolayer of large spheres was prepared. If the quantity of the small spheres used is equal to the intersites in large spheres, one small particle should exclusively settle within the intersite between three large spheres, forming a LS_2 structure, as shown in Fig. 1b. Similarly, the complex and beautiful colloidal patterns, such as LS_3, were obtained by using this method (Fig. 1c and d).

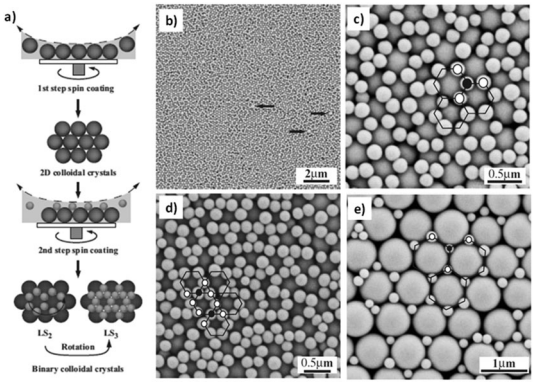

Fig. 1 (a) Illustration of the procedure used to fabricate binary colloidal crystals by stepwise spin-coating. (b) Low-magnification SEM image of the binary colloidal crystals consisting of 442 nm and 222 nm silica spheres produced by stepwise spin-coating at a spin speed of 3000 rpm, where large spheres are indicated by arrows, and high-magnification SEM micrographs of the regions consisting of LS_2 (b) or LS_3 (c), where circles (solid or empty) mark locations of 222 nm spheres and the polygon frames highlight their pattern. (d and e) SEM images of the binary colloidal crystals by stepwise spin-coating at a spin speed of 3000 rpm, in which 222 nm silica spheres were confined within the intersites between hexagonally close-packed 891 nm silica spheres. Reproduced from *Adv. Mater.*, 2004, **16**, 244. Copyright 2004, Wiley-VCH.[96]

The conceptual design in spin-coating is very important for fabrication of ultrathin nanofilms. Very recently, Kirihara *et al.* reported a novel thermoelectric (TE) concept based on the spin Seebeck effect,[98–102] called ''spin-thermoelectric (STE) coating''. An ultrathin STE-coating layer (only 0.01% of the total sample thickness) can be fabricated using the STE coating on a non-magnetic substrate. A spin-current-driven TE conversion was successfully demonstrated under a temperature gradient perpendicular to such ultrathin films. It includes three fabrication steps (Fig. 2a). First, a metal–organic decomposition (MOD) method was used to fabricate a bismuth-substituted yttrium iron garnet (Bi:YIG) on the $Gd_3Ga_5O_{12}$ (GGG) substrate. The MOD method is composed of two steps: coating, followed by annealing of the MOD solution containing the constituent elements.[103–105] Finally, a Pt film was sputtered on the whole area of the Bi:YIG. Fig. 2b shows a clear cross-section in which the crystalline Bi:YIG film was successfully formed on the GGG substrate with a coherent interface. The thicknesses of the GGG substrate, Bi:YIG film and Pt film are 0.7 mm, 60 nm and 10 nm, respectively. Another advantage of this method is the ease in large-area manufacturing, because it does not require patterning steps such as photolithography. If there is a temperature difference ($1T$) between the top of the Pt film and the bottom of the GGG substrate, TE conversion will take an effect (Fig. 2c). Namely, a spin current density at the Pt/Bi:YIG interface perpendicular to the plane is driven by the temperature gradient as a result of the SSE.[106–108] Such a versatile implementation of the TE function may pave the way for novel applications making full use of omnipresent heat.

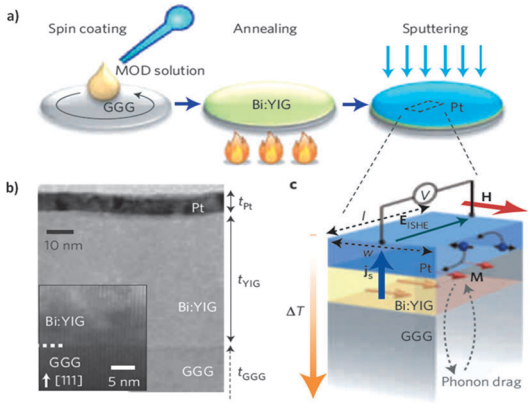

Fig. 2 Demonstration of the STE coating: (a) schematic of the STE-coating process. The Bi:YIG film was formed by spin-coating the MOD solution, with subsequent annealing. Following this the Pt film was sputtered. (b) Cross-sectional TEM images of the STE-coated sample, composed of Pt and Bi:YIG films on a $Gd_3Ga_5O_{12}$ (111) substrate (t_{Pt} = 10 nm, t_{YIG} = 60 nm, and t_{GGG} = 0.7 mm). The inset clearly shows a coherent Bi:YIG/GGG interface. (c) Spin-current-driven TE conversion in the STE coating. Here $1T$ represents the temperature difference applied across the entire sample thickness (including the substrate). In this set-up, the spin current j_s is driven perpendicularly to the Pt/Bi:YIG interface and then converted into an electric field EISHE as a result of the ISHE in Pt. Reproduced from *Nat. Mater.*, 2012, **11**, 686. Copyright 2012, Nature.[98]

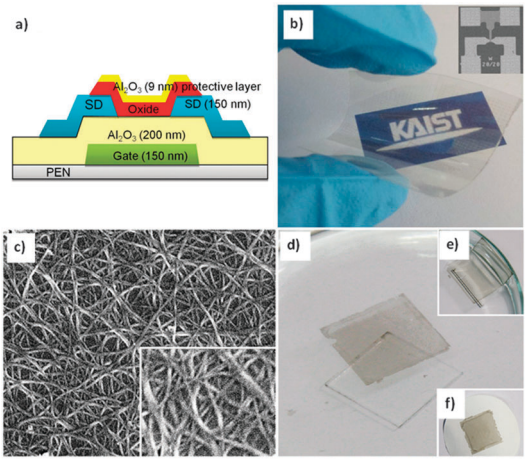

Fig. 3 (a and b) Characterization of flexible IZO:F TFT on PEN film annealed at 200 °C: (a) the cross-sectional image of a channel region (150 nm ITO gate/200 nm Al_2O_3 gate dielectric/150 nm ITO SD/5 nm IZO:F active layer at 200 °C 2 h/9 nm Al_2O_3 passivation), and (b) a picture of flexible IZO:F on a PEN film substrate (inset picture is an SEM image of the channel region). Reproduced from *Sci. Rep.*, 2013, **3**, 2085. Copyright 2013, Nature.[108] (c) SEM images of SWCNT network film. The film was prepared by spin coating in the presence of 5TN-PEG, and then 5TN-PEG was removed by dipping in dichloromethane and water followed by chemical treatment with HNO_3 and $SOCl_2$. Inset shows a highly magnified image of the network structure. (d–f) Photographs of free-standing films: (d) floating on the water surface, (e) releasing from the glass substrate, and (f) transferring to filter paper. Reproduced from *ACS Nano*, 2010, **4**, 5382. Copyright 2010, American Chemical Society.[109]

Nowadays, nanofilms with flexible and/or transparent characteristics are paid more and more attention, because they may widely be used as electrodes for light-emitting diodes or photovoltaic devices. For example, Bae *et al.* demonstrated transparent flexible fluorine-doped indium zinc oxide (IZO:F) thin-film transistors (TFTs)[108] obtained by a spin-coating method of the metal fluoride precursor aqueous solution after annealing at 200 °C for 2 h on polyethylene naphthalate films (Fig. 3a). In the IZO:F thin films, a free electron or an oxygen vacancy site eliminating an electron trap site are generated because of substitution of a fluorine atom to an oxygen atom. The doped fluorine can simultaneously enhance the mobility and improve the gate bias stability of the TFTs. A transparent IZO:F TFT was also implanted on a flexible PEN film. Fig. 3a and b displays a schematic diagram of the device structure and a photograph of the fabricated transparent flexible TFT. It can be seen that Al_2O_3 thin films fabricated by atomic layer deposition (ALD) are sandwiched between a 200 nm gate dielectric layer and a 9 nm passivation layer.

Recently, many promising materials, such as single-walled carbon nanotube (SWCNT) films have attracted decent attention as an alternative to metal oxide electrodes due to their unique electrical conductivity, excellent mechanical properties, and feasibility of solution process. They also satisfy the industrial demand for flexible and low-cost electrodes.[110] For example, Jo *et al.* reported the synthesis of high-quality SWCNT films *via* a simple spin-coating method. In the fabrication process, oligothiophene-terminated poly(ethylene glycol), a non-ionic and amphiphilic surfactant, were used.[109] The presence of this kind of surfactant guaranteed the formation of a dense network of SWCNTs on the substrate due to the absence of charge repulsion between SWCNT–surfactant complexes. In addition, the film can be used as a transparent electrode in flexible optoelectronic devices. As shown in Fig. 3c, there is no directional orientation of the nanotubes, unlike that mentioned in earlier reports.[111–113] Therefore, a uniform network consisting of individual SWCNTs was formed. Another advantage of these as-made films is dimensional stability. When a SWCNT film is floated on water, it is easily released from its substrate and can be transferred to another substrate. This "free-standing" SWCNT film can be easily used in microelectronics.[114] Especially, it is possible to realize flexible electrical devices, if the SWCNT film is transferred on a flexible substrate, such as polyethylene terephthalate (PET) and polydimethylsiloxane. Fig. 3d–f presents the photographs of the free-standing film. It is found that transference of this free-standing film onto another substrate can be easily carried out when the film is immersed into deionized water: the film is floated on the water surface and then released from the glass (Fig. 3d and e). Also the high bending stability is natural for this freestanding film.

3.2 Electrospinning route

Electrospinning is a promising technique for creation of diverse forms of fibrous assemblies and individual fibers with hierarchical structures, especially, nanofilms. Some of these film-like structures display a remarkable resemblance to the materials and objects existing in nature, such as honeycombs, spider webs, extracellular matrices, plant tendrils and leaves, *etc.* This section gives a brief introduction to the recent use of electrospinning for creation of nanofilms.

Since recently, electrospinning has been regarded as a powerful technique to fabricate 1D micro/nanostructures. This method can effectively control the composition and topology of products, enabling improved performance in numerous applications.[115–119] Despite many metrics of electrospinning methodologies, easiness, versatility, and rapidity, there are still many drawbacks of this traditional method. For example, it remains a big challenge to prepare transparent conducting electrodes, which are essential components for numerous flexible optoelectronic devices, including touch screens and interactive electronic components.[120–122] In addition, a lot of toxic or corrosive organic solvents are needed during the preparation of starting materials. This contradicts with the urgent requirements for energy-saving and environmental protection. A perfect example is a thin film of indium tin oxide, a prototype transparent electrode material.[123] Although flexibility is greatly improved due to the addition of conducting polymers,[124] carbon nanotubes[125–127] and graphene,[128–130] the optoelectronic performance of these carbon-based materials is limited by low conductivity.[131–139] Up to now, the resistances of nanofilms are also less than 10 Ω m^{-1} at 90% transmission even for the metal nanowire-based electrodes.[132–139] Hence, establishing efficient and facile synthesis protocol to tackle these issues would be of great benefit toward large scale film production and growing application demands.

Very recently, Cui's group[140] presented a facile fabrication process resulting in a new type of transparent conducting electrode that shows both a superior optoelectronic performance (sheet resistance of $\sim$2 Ω m^{-1} at 90% transmission) and remarkable mechanical flexibility under both stretching and bending deformations. The electrode consists of a free-standing metallic nanotrough network and is produced by combination of electrospinning and metal deposition. Therefore, this transparent conducting electrode is rather practical. Fig. 4a shows the fabrication process of the nanotrough network[140] based on templating ultralong polymer nanofibres. Firstly, electrospinning is used to prepare continuous polymer nanofibre webs.[141] Secondly, standard thin-film deposition techniques[142] are used to coat a thin layer of material onto the free-standing polymer nanofiber networks (Fig. 4b). This ensures a rich variety of functional materials while retaining a bulk-like electrical conductivity. As illustrated in Fig. 4c, nanotroughs have a concave cross-section form due to the directionality of these deposition processes. In addition, the coated polymer fibers can easily be transferred onto various substrates because of their mechanical flexibility and robustness. Thirdly, when the entire electrode is submerged in water or other organic solvents, the polymer templates can be removed. As shown in Fig. 4b–d, continuous nanotrough networks may be fabricated from a wide variety of functional materials, including silicon, indium tin oxide (ITO) and metals, such as gold, silver, copper, platinum, aluminium, chromium, nickel and their alloys. It is also noted that individual nanotroughs are naturally interconnected at their junctions during metal deposition (Fig. 4b). Concave cross-sections (Fig. 4c) are seen from a side-view SEM image of the as-made nanotroughs. As shown in Fig. 4d, gold nanotroughs can successfully be attached to different surfaces,

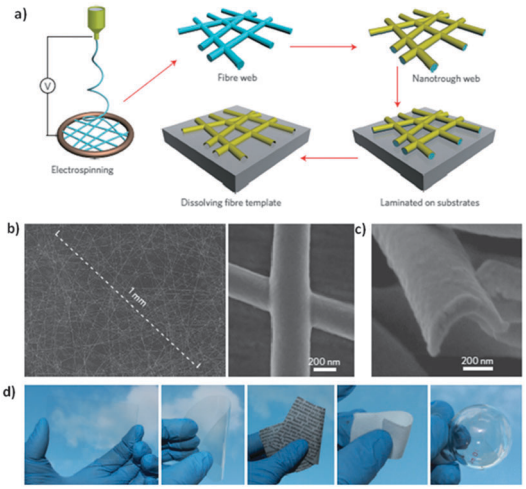

Fig. 4 Fabrication and transfer process of nanotroughs. (a) Schematic of the polymer-nanofibre templating process for fabricating nanotroughs. Polymer nanofibre templates were first prepared by electrospinning, then coated with selected materials using standard thin-film deposition techniques. The coated fibers were transferred onto a solid substrate. The substrate was subsequently dipped in water or an organic solvent to dissolve away the polymer-fiber template. (b) Top-view SEM images of gold nanotrough networks (left) and a junction between two nanotroughs (right). (c) SEM image of the cross-section of a single gold nanotrough, revealing its concave shape. (d) Gold nanotrough networks can be transferred easily onto various substrates, including a glass slide, PET plastic, paper, textile and a curved glass flask (left to right). Reproduced from *Nat. Nanotechnol.*, 2013, **8**, 421. Copyright 2013, Nature.[140]

including a glass slide, polyethylene terephthalate (PET) plastic, paper, a textile and a curved glass flask, all without any surface treatment. This makes all the surfaces highly conducting. Note that the nanotroughs are attached to the substrates so firm that they cannot be peeled off with a Scotch tape.

Very recently, Liang and co-workers[143] have reported a facile and cost-effective way to prepare nanofilms consisting of 1D porous carbon microfibers by using an electrospun fiber-like natural product, *i.e.*, silk cocoon, as precursor. Fig. 5a is the schematic illustration of the natural electrospinning-like process, in which the silkworm spins silk microfibers to form a cocoon around itself. Then, the electrospun fiber-like natural cocoon microfibers can be directly transformed into 6 mm of 1D carbon microfibers (Fig. 5b and c) after a simple carbonization treatment. The 1D carbon microfibers consist of numerous carbon nanoparticle units of 10–40 nm in size, which are interconnected with each other to form a unique 3D porous network structure. These carbon units exhibit various porous structures, such as microporous, mesopores and macropores. Note that in the past, the fabrication of porous network structures required fussy and multiple synthetic steps including reaction-induced phase separation and supercritical drying.[144] Therefore, in this method, the employment of a low-cost and environmentally friendly silk cocoon as a carbon source avoids many chemical reactions and physical processes persistent to normal procedures for fabrication of 1D porous carbon fibers.[145] Another important characteristic of the carbonized cocoon is that it is easily tailored into various forms, *e.g.* rectangular felt (Fig. 5d). To test its

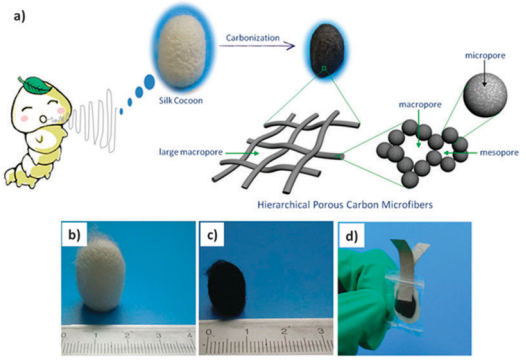

Fig. 5 (a) Schematic illustration of the fabrication of hierarchical porous carbon microfibers from a silk cocoon. (b–d) Photographs of the silk cocoon before (b) and after (b) carbonization, (c) the as-fabricated binder-free film as a supercapacitor. Reproduced from *Sci. Rep.*, 2013, **3**, 1119. Copyright 2013, Nature.[143]

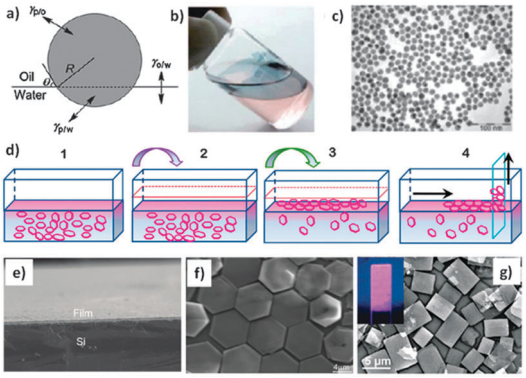

Fig. 6 (a) An isotropic particle at the oil–water interface, showing the interfacial tensions between the particle and oil, the particle and water, and the oil and water, respectively. Reproduced from *Angew. Chem., Int. Ed.*, 2010, **49**, 10052. Copyright 2011, Wiley-VCH.[154] (b) Left: an aqueous gold soln. (pink) covered with heptane (colorless); centre and right: after the addition of 4 mL ethanol to the soln., a gold nanocrystal layer (blue) is formed at the heptane–water interface and extends up the heptane–glass interface. Gold nanocrystals are extracted from the water phase, but do not transfer to the heptane phase. (c) TEM image of a layer with maximum coverage (65%) collected from the heptane–water interface shows that the layer does not contain 3D aggregates, the voids have a typical size equivalent to 1–10 nanocrystals; the space between particles is 1–4 nm. Reproduced from *Angew. Chem., Int. Ed.*, 2004, **43**, 458. Copyright 2004, Wiley-VCH.[151] (d–f) SEM images of monolayer films using $Co(OH)_2$ platelet crystallites of different lateral sizes: ~4 and ~2 μm; (d) schematic illustration of the hexane/water interfacial self-assembling procedure. Step 1: preparing an aqueous suspension of hexagonal platelet crystallites in a Langmuir trough. Step 2: adding hexane to form a hexane/suspension interface. Step 3: injecting alcohol to trap the platelet crystallites to the hexane/suspension interface, forming a monolayer film. Step 4: after hexane is evaporated or extracted, the monolayer film can be transferred to a substrate in vertical lifting method. (d) Pressure–area (π–A) curve for the film transfer under a constant surface compression pressure of 15 mN m^{-1}. For the abscissa axis, the percentage of surface relative to the area before compression and film transfer is used. (f) Photograph (left panel) and cross-section SEM image (right) of continuous monolayer film deposited on a Si substrate. Reproduced from *Chem. Mater.*, 2010, **22**, 6341. Copyright 2010, American Chemical Society.[155] (g) Gd_2O_3:0.05 Eu film. The inset shows the red-light emission of the precursor hydroxide film and oxide film under UV irradiation. Reproduced from *Angew. Chem., Int. Ed.*, 2009, **48**, 3846. Copyright 2009, Wiley-VCH.[86]

feasibility for practical applications, the silk cocoon-based HPCMF in the form of rectangular felt has directly been used as a binder-free electrode for a supercapacitor. It shows a good capacitive performance. The interpenetrated fiber network texture combined with the hierarchical nanoporous structure in the carbon fiber framework guarantees quick penetration of electrolytes, thus decreasing the resistance for the ion transfer.[146–148] Moreover, it is believed that the plentiful nitrogen functional groups in the carbon framework can simultaneously realize the improved wettability of the as-prepared material in the electrolyte and the good pseudocapacitance.[149,150]

3.3 Some recently reported novel strategies

Although the traditional methods can significantly decrease the manufacturing cost, they also usually need special equipment and are time-consuming. Furthermore, high-quality thin films could be achieved from these wet-chemical methods only for some peculiar nanostructures. Therefore, it is still highly desirable to develop new and simple approaches for the fabrication of high-quality nanofilms. In this section, we introduce some new wet-chemical strategies for nanofilm fabrication, which include oil–water self-assembly, the liquid–liquid interface strategy, the magic "magnetic ink" method, two-dimensional oriented attachment, electrochemical Li-intercalation and exfoliation, sonication in various solvents, *etc*.

3.3.1 Oil–water self-assembly. Since a discovery by Vanmaekelbergh *et al.* in 2004,[151] oil–water interfacial self-assembly has been used as a novel strategy for various nanofilms. This novel strategy effectively opens the door for the self-assembly of hydrophilic nanostructures into closely-packed nanofilms. More importantly, Wu's and our groups have developed this self-assembly as a novel and facile strategy to fabricate nanofilm-based devices,[1–4,30,31,37,43,152,153] such as photodetectors, and electrical resistive switching devices. Herein we shortly discuss the thermodynamic mechanism of the oil–water interfacial self-assembly, then we focus on the self-assembly of various low-dimensional building blocks at an oil–water interface developed so far to fabricate high-quality nanofilms.

As illustrated in Fig. 6a, a proportion of the initial oil–water interface is replaced by the nanoparticle–oil interface after the entrapment of one spherical crystallite at the oil–water interface. There are three contributions for the total energy change for this process, from the particle–oil, particle–water and nanoparticle/water interfaces, respectively. The total energy (Helmholtz free energy) change ΔE can be expressed as follows:[156,157]

$$\Delta E = -\pi R^2[\gamma_{OW} - (\gamma_{PW} - \gamma_{PO})]^2/\gamma_{OW} < 0 \qquad (1)$$

where γ_{PW}, γ_{PO}, and γ_{OW} are the interfacial tensions between the particle and water, the particle and oil, and the oil and water, respectively. R represents the radius of a spherical nanoparticle. It is obvious that the interfacial assembly of nanoparticles is driven by a minimization of the Helmholtz free energy. That is, the size of particle and the wettability of the particle surface are the two main factors for ΔE. ΔE is directly proportional to R^2,

so, ΔE is more sensitive to a particle's size and thus the assembly for larger nanoparticles is more stable than that for the smaller ones.[158,159] That is, the thermal energy for large-sized particles, k_BT, is much smaller than the decrease in the total energy per particle, so the particles are strongly held on the liquid–liquid interface.

As shown in Fig. 6b, a clear two-phase region can be seen, the aqueous gold soln. with pink color and an immiscible layer of heptane. When ethanol is added into the gold soln., a blue layer immediately forms at the heptane/water interface. Note that the as-made film at the interface is very stable and does not easily collapse. And there is a high coverage (65%) for the film obtained at the oil–water interface (Fig. 6b). Furthermore, this film could be transferred easily onto various solid substrates through horizontal or vertical lifting after removing the oil layer by spontaneous evaporation.

Fig. 6d–f depicts an example of the nanofilm obtained by using an oil/water interfacial self-assembling procedure, in which a monolayer film of $Co(OH)_2$ platelet crystallites was fabricated.[155] A schematic illustration of the procedure is shown in Fig. 6d. 80 mg of $Co(OH)_2$ pink suspension was firstly prepared and then poured into a Filgen LB40-KBC Langmuir trough equipped with a Wilhelmy balance. At the same time, there is a contact angle $<90^\circ$ formed at hexane/water interface. When butanol is added, the contact angle approaches 90° due to the change in surface energy. As a result, an oriented monolayer of the platelet crystallites forms at the interface. Fig. 6d displays a side-view SEM image of as-made $Co(OH)_2$ films under a surface compression pressure of 15 mN m^{-1}. As shown in Fig. 6f, a close-packed monolayer film is formed on a large area, in which hexagonal platelets are well ordered and tiled with their edges in contact, basically side-by-side. Therefore, a highly-oriented film with high area coverage ratio and smooth surface can be produced by the oil–water interfacial self-assembly of 2D nanostructures. In addition, multilayer $Eu(OH)_{2.5}Cl_{0.5}\cdot 0.9H_2O$ platelet films[86] have successfully been synthesized using a similar self-assembly mechanism. As-obtained $Eu(OH)_{2.5}Cl_{0.5}\cdot 0.9H_2O$ platelet films exhibit the typical Eu^{3+} luminescence properties, while the intensity of the emission peaks at 701 nm increases roughly in proportion to the number of layers.

3.3.2 Ultrathin nanocrystalline films at the liquid–liquid interface. Another simple but elegant means of generating ultrathin nanocrystalline films are based on the reaction at the organic–aqueous interface, namely the liquid–liquid interface.[160–162] Rao's group has made great progress in the field and prepared a series of ultrathin nanocrystalline films of metals[163–169] such as gold,[164–167] silver[168] and alloys[169] as well as of inorganic materials[163,170–175] such as semiconducting metal chalcogenides (*e.g.*, HgSe,[162] CuO,[172] CuS,[172] ZnS,[173] CuSe[174]) and oxides by using this mechanism. Different from the above-mentioned oil–water self-assembly by using hydrophilic building blocks, this method is primarily based on the reaction occurring at the interface giving rise to a film at the interface. That is, a metal organic compound will be dispersed in the organic layer and a reducing, a sulfiding, or an oxidizing agent is injected in the aqueous layer. Based on the detailed experiments, Rao *et al.* explained how the various reaction parameters affected the films formed at the interface and how alkanethiols led to the disintegration of the films.[160] It should be noted that some single-crystalline films such as metal chalcogenides can be obtained at the interface.

It is simple and straightforward to prepare materials in the form of nanocrystalline films by using this method.[160] In a general synthesis, Na_2S is utilized as the source of sulphur for making nanocrystalline films of metal sulfides, while Na_2Se or *N,N*-dimethylselenourea are used as the starting materials of selenium to fabricate metal selenide films. Taking as an example, very recently, Rao *et al.* have employed this strategy for room temperature synthesis of HgSe and $Hg_{0.5}Cd_{0.5}Se$ nanocrystalline films at the toluene–water interface.[162] In a typical preparation of HgSe nanocrystalline films, 25 mg of $Hg(cup)_2$ in 20 mL toluene is allowed to stand in contact with a 20 mL water solution containing 6.5 mg of selenourea in a 50 mL beaker at room temperature. For the similar synthesis of $Hg_{0.5}Cd_{0.5}Se$ films, the precursors are 7.1 mg of selenourea and 25 mg of $Hg_{0.5}Cd_{0.5}(cup)_2$, respectively. After slow addition of the toluene solution along the walls of the beaker containing an aqueous solution of selenourea, the formation of the nanocrystalline film at the interface is very rapid and occurs within a few minutes. From the photographs shown in Fig. 7a and d, the nanocrystalline films indeed formed at the toluene–water interface. Their TEM, HRTEM and corresponding selected area electron diffraction (SAED) patterns (Fig. 7b and e) indicate that these films consist of numerous HgSe and $Hg_{0.5}Cd_{0.5}Se$ QDs. The *d*-spacing of 0.21 nm (Fig. 7c) agrees well with the (220) crystal planes for HgSe and a spacing of 0.34 nm (Fig. 7f) corresponds to the (111) planes of $Hg_{0.5}Cd_{0.5}Se$. The mean sizes are $\sim$9 nm for HgSe and $\sim$5 nm for $Hg_{0.5}Cd_{0.5}Se$ QDs, as illustrated on the size distribution histograms shown as insets in Fig. 7c and f. It is worth noting that the nanocrystalline films exhibit the dense nature, which can ensure electronic coupling between the nanodots and provide a continuous channel for the unimpeded transport of carriers across the film.[175] As a result,

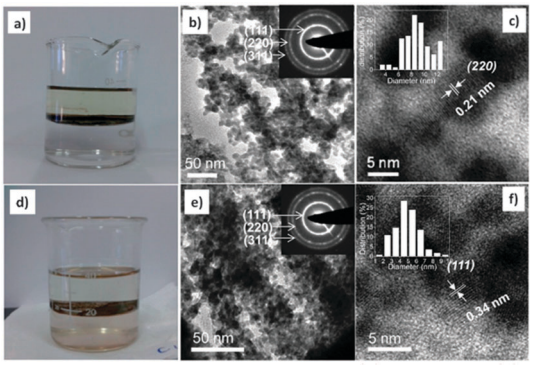

Fig. 7 (a and d) Photographs of nanocrystalline films of (a) HgSe and (d) $Hg_{0.5}Cd_{0.5}Se$ QDs formed at the toluene–water interface. (b) TEM and (c) HRTEM images of HgSe QDs. (e) TEM and (f) HRTEM images of $Hg_{0.5}Cd_{0.5}Se$ QDs. The insets in (b) and (e) are SAED patterns and the insets in (c) and (f) are particle size histograms. Reproduced from *J. Mater. Chem. C*, 2013, **1**, 6184. Copyright 2013, Royal Society of Chemistry.[162]

such strong inter-particle connectivity will be helpful or crucial for a good photoconduction of an as-made photodetector device, since the interfacial barriers across particles give rise to transport-noise, thus decreasing the device performance. It is also believed that this method can be adopted for not only generating nanocrystalline films of various materials but also to study processes occurring at the liquid–liquid interface.

3.3.3 "Magnetic ink" nanofilms. In order to better meet ever-growing needs, especially in printing, new techniques for the preparation of new kinds of nanofilms should be developed. Among them, photonic printing and inking are important technical extensions of responsive photonic crystals. This is because the structural colors are more durable for photonic crystal structures than for traditional pigments and dyes. However, considering recording and energy-saving, the photonic structure should maintain its multiple color states.[176,177] In addition, there are some limitations, even for fully-developed ink-jet printing techniques, such as the complex pre-treatment of the paper surface, low flexibility of usable substrates, relatively high cost owing to its non-reusable nature, the inevitable crystal defects, and consequent inhomogeneous colors. These defaults must result in environmental disturbance during the assembly process.

Very recently, Kwon and co-workers demonstrated a fast and high-resolution color printing technique by combining magnetically tunable photonic structures with maskless lithography techniques.[178] In that work, a magnetic ink ("M-ink"), a three-phase mixture consisting of superparamagnetic Fe_3O_4@-SiO_2 colloids, a solvation liquid, and a photocurable resin, were used. Fig. 8a and b is the schematic illustration of the production of high-resolution multiple structural colors using a single material. Once an external field is applied, the chain-like structures are formed from the magnetic colloids in the M-ink film. And then they are fixed in the polymer matrix with a periodic arrangement by the subsequent UV exposure. As a result, the structural color is fixed. A spatially modulated focused UV beam was used as the "printing" tool to realize high-resolution patterning of multiple structural colors. And the color of each exposed spot can be precisely tuned by using the programs of the high-speed optical projection and magnetic field strength modulation. Moreover, maskless lithography can be used for creating arbitrary microscale patterns because of the instantaneous nature and thus the localized solidification. With assistance of a microelectro-mechanical system (MEMS)-based spatial light modulator, instantaneous illumination (<80 ms) with patterned UV light can be applied for curing the resin. In theory, by using a sequential process involving cooperative actions of magnetic field modulation and spatially controlled UV exposure, a single ink can generate various multicolored patterns. Fig. 8c–f shows some examples of micro-patterns with different structural colors and geometries, which have been produced by repeating this "tuning and fixing" process. Note that there is no need to move the substrate during the preparation process, since only one M-ink (instead of multiple color inks) was deposited at the beginning of the process. Furthermore, by modulating the number of color dots and presenting similar grayscale effects, the overall reflection intensity can also controlled. Besides, it is possible to realize the parallel distribution of dots with different structural colors for the spatial color mixing. In addition, when their sizes are below the resolution of the human eye, quantized dot arrays consisting of different colors can be regarded as a single mixed color.

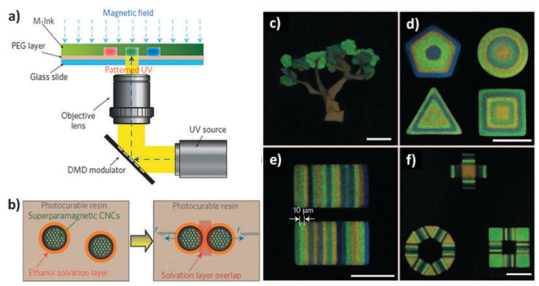

Fig. 8 (a) Schematic of the production of high-resolution multiple structural colors with a single material. (a) Maskless lithography setup for color fixing. Instantaneous exposure using patterned UV light reflected from a digital micromirror array (DMD) modulator allows the fast production of structural color. (b) The superparamagnetic core and ethanol solvation layer allow the stable dispersion of the CNCs in the M-ink. A strong repulsive force can be generated when two solvation layers overlap. (c–f) Printing of high-resolution patterns with multiple structural colors including (c) a tree, (d) concentric triangles, squares, pentagons, and circles, (e) bar codes, and (f) composite patterns of strip and polygon. Scale bars are 250 mm (c and f) and 100 mm (d and e). Reproduced from *Nat. Photonics*, 2009, **3**, 534. Copyright 2009, Nature.[178]

A more general strategy for photonic printing is to define patterns on the preformed photonic crystal film. In order to create a contrast of diffraction color in the form of letters and patterns, various methods can be introduced into these printing processes. For example, if photolithography techniques are used, a liquid-crystal infiltrated inverse opal film by UV-induced LC phase transition can be tuned. In addition, if photoisomerization-induced polymer expansion and contraction occurs, the printing can also be realized.[179] It is therefore believed that this technique will provide a new platform for full-color structural printing with fine resolution.

3.3.4 Oriented attachment strategy. Different from the self-assembly process discussed above, the 2D oriented attachment strategy requires the small inorganic building blocks to be connected with each other in a confined 2D space. Therefore, a common crystallographic face is shared to further minimize their high surface energy, and thus there is a thermodynamic balance for the formation of atomically thick 2D crystals.[180–186] Therefore, 2D oriented attachment of the small building blocks is regarded as the exclusive way to achieve the atomically-thick 2D nanofilms, because there is a lack of an intrinsic driving force for 2D anisotropic growth. Up to now, a variety of 2D ultrathin nanofilms with non-layered structures, such as, PbS,[180] Co_9Se_8,[181] CeO_2,[182] and so on, have been prepared *via* this strategy. Accordingly, the atomically thick 2D crystals of layered structural materials, such as SnSe,[183] Bi_2Se[187] *etc.* can also be successfully achieved, as predicted.

As a representative case, the atomically thick PbS nanosheets[180] with unique lamellar stacking are discussed based on a standard synthetic procedure for generation of PbS nanoparticles. Then the

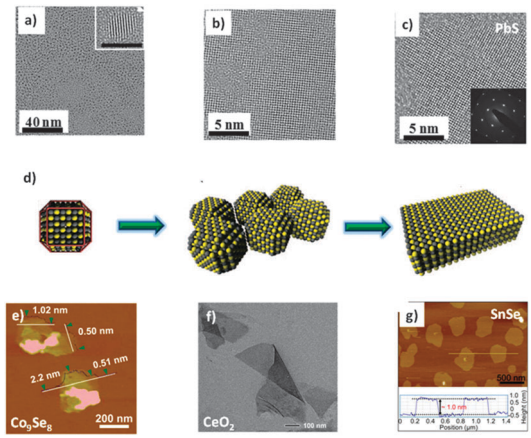

Fig. 9 Atomically thick 2D crystals synthesized by oriented attachment. (a–c) Morphology evolution of PbS nanosheets at different reaction times. (d) Schematic illustration of the oriented attachment from nano-sized building blocks to ultrathin nanosheets. Reproduced from *Science*, 2010, **329**, 550. Copyright 2010, AAAS.[180] AFM images of (e) Co_9Se_8 and (g) SnSe, TEM image of (f) CeO_2. (e) Reproduced from *J. Am. Chem. Soc.*, 2012, **134**, 11908. Copyright 2012, American Chemical Society.[181] (f) Reproduced from *Angew. Chem., Int. Ed.*, 2010, **49**, 4484. Copyright 2010, Wiley.[182] (g) Reproduced from *J. Am. Chem. Soc.*, 2013, **135**, 1213. Copyright 2013, American Chemical Society.[183]

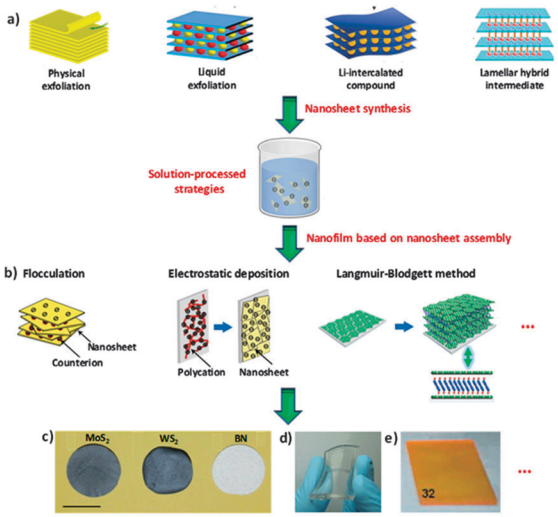

Fig. 10 (a) Schematic model illustrating several ultrathin nanosheet synthesis strategies: physical exfoliation, liquid exfoliation with the help of different ions, the chemical exfoliation of Li-intercalated compound and lamellar hybrid intermediates. Reproduced from *Adv. Mater.*, 2010, **22**, 5082. Copyright 2010, John Wiley and Sons.[189] Reproduced from *Science*, 2011, **331**, 568. Copyright 2011, AAAS.[190] Reproduced from *Angew. Chem., Int. Ed.*, 2011, **50**, 11093. Copyright 2011, John Wiley and Sons.[191] Reproduced from *Nat. Commun.*, 2012, **3**, 1057. Copyright 2012, Nature.[192] (b) Schematic of various assembling methods for nanosheets: flocculation, electrostatic sequential adsorption, Langmuir–Blodgett method. Reproduced from *Adv. Mater.*, 2010, **22**, 5082. Copyright 2010, John Wiley and Sons.[189] Reproduced from *Chem. Rev.*, 2012, **112**, 4124. Copyright 2012, American Chemical Society.[193] (c) Solution-processed, free-standing films of randomly arranged nanosheets of h-BN, MoS_2, and WS_2. Scale bar, 25 mm. Reproduced from *Science*, 2011, **331**, 568. Copyright 2011, AAAS.[190] (d) Transparent and flexible graphene films on the PDMS substrates. Reproduced from *Nature*, 2009, **457**, 706. Copyright 2009, Nature.[190] (e) Photograph of an ultrathin $(SPT/LDH)_n$ (n = 4–32) film with 32 bi-layers when exposed to daylight. Reproduced from *AIChE J.*, 2011, **57**, 1926. Copyright 2011, AIChE.[194]

original particles (Fig. 9a) can be fused into aggregates (Fig. 9b). A lot of {110} surface planes are present in an individual particle, which can be identified due to an angle of 135° for its crystalline edges. A close inspection of Fig. 8b indicates that nanocrystals are fused into nanofilms in two dimensions. Finally, the structure of PbS nanocrystals merges into PbS sheets, as shown in Fig. 9c. Fig. 9d depicts a general route to fabricate such a nanofilm. Note that the shape of the original particle is a truncated cuboctahedron with 6 {100}, 8 {111}, and 12 {110} facets. Upon crystal growth, the particles try to minimize the most energetically unfavorable surface facets by fast growth perpendicular to the respective facet. By using similar strategies, other materials with few-layered structures including Co_9Se_8,[181] SnSe,[182] and CeO_2[183] were also obtained (Fig. 9e–g). It is worthy to note that the superfine changes of the reaction conditions, such as, reaction temperature, the concentration of materials, the solvents *etc.* will affect the oriented attachment process. Therefore, one needs to well modulate the reaction parameters to critically optimized conditions, ensuring that the small building blocks are directionally assembled in a confined 2D space.

3.3.5 Nanofilms based on nanosheet assembly. The discovery of graphene in 2004 by Andre Geim and Konstantin Novoselov,[188] resulted in an explosive interest in two-dimensional materials, namely, nanosheets. A number of methods have been developed. As shown in Fig. 10, these involve physical exfoliation,[189] liquid exfoliation with the help of different ions,[190] chemical exfoliation of a Li-intercalated compound[191] and lamellar hybrid intermediates,[192] oxidation, or surface passivation by solvents. As an example, a gelation method used for the synthesis of the titanium oxide nanosheet suspension may be mentioned.[195] Upon freeze-drying there is a limited number of nanosheets restacked, thus a thin lamella, tens of nanometers thick and tens of micrometers in lateral size, is formed. After heat treatment above 400 °C, anatase nanosheets are obtained, retaining a thin flaky morphology. Another effective route for the synthesis of nanosheets is the liquid exfoliation method developed by Coleman *et al.*[190] It mainly includes three steps. The first one is an ion intercalation process. Ions are intercalated between the layers in a liquid environment, swelling the crystal and weakening the interlayer attraction; and then agitation (such as shear, ultrasonication, or thermal) completely separates the layers, resulting in an exfoliated dispersion. The second step is based on ion exchange. Some layered compounds contain ions between the layers so as to balance surface charge on the layers. These ions can be exchanged in a liquid environment for other, often larger ions. The agitation results in an exfoliated dispersion. The final step is a sonication-assisted exfoliation process. The layered crystals are sonicated in a solvent, leading to exfoliation and nanosheet formation. It is quite important to choose the exact solvents. If "good" solvents, those with the appropriate surface energy, are chosen, the exfoliated nanosheets are stabilized against re-aggregation. Otherwise, for "bad" solvents re-aggregation and sedimentation would occur. One of the most

effective methods for the mass production of fully exfoliated nanosheets is the ultrasound-promoted hydration of lithium-intercalated compounds.[190–195] The cut-off voltage is used to optimize the electrochemical lithiation conditions for the preparation of few-layered BN, $NbSe_2$, WSe_2, Sb_2Se_3 and Bi_2Te_3. In the lithium intercalation process, the formation of a Li_xXS_2 compound is an important step, whereas the yield of monolayers turns out to be tuned by controlling this reaction. And recently there are some new solution-processed routes to fabricate nanosheet-constructed inorganic materials.[196–200]

It is worth noting that there are large quantities of nanosheets present in the liquid dispersions. Therefore, it is easy to prepare thin films and composites consisting of such nanosheets. In particular, 2D nanosheets are capable of forming highly oriented films by aligning them parallel to the substrate surface. As a result, some wet-processing film fabrication techniques can be used with the advantage of relatively easy nanosheet handling.[201] Typical assembling processes for nanosheets, flocculation and layer-by-layer (LBL) assembly, are schematically illustrated in Fig. 10b. With the charged feature, flocculation is a very easy protocol for fabricating micro- and mesoporous lamellar nanofilms consisting of nanosheets. On the other hand, multilayer nanofilms on a planar or curved surface can be designed and built up through the most frequently utilized electrostatic sequential adsorption and Langmuir–Blodgett (LB) deposition. In addition, processing from liquids allows the deposition of individual nanosheets on surfaces and formation of thin or free-standing films. Photographs of free-standing films are presented in Fig. 10c, BN, MoS_2, and WS_2 films are obtained by filtration or spraying, their thickness ranges from a few nanometers to hundreds of micrometers.

There is a high need to prepare transparent and flexible films. Very recently Hong and co-workers developed a dry-transfer process for making a graphene film using a soft substrate, such as a polydimethylsiloxane (PDMS) stamp.[128] The PDMS stamp was firstly attached to the CVD-grown graphene film on the nickel substrate. And then the nickel was removed away using $FeCl_3$, only the adhered graphene film is left on the PDMS substrate. Therefore, various sizes and shapes of graphene films can be transferred to an arbitrary substrate. Consequently, fabrication of large-scale graphene electrodes and devices can be realized by using this useful dry-transfer process without additional lithography processes (Fig. 10d). Similarly, by using the LBL method, the luminescent organic anions can be assembled with the layered double hydroxides (LDHs) nanosheets to prepare luminescent materials. As a result, the LDH-based ultrathin films with individual colors were fabricated. For example, by assembling the sulfonated polythiophene (SPT) and Mg–Al LDH nanosheets LBL, a red luminescent thin film was produced,[194] as shown in Fig. 10e, after each bilayer cycle. Note that the color intensity of the thin film gradually increased with the increase of the bilayer numbers.

3.3.6 Practical nanoporous films based on a dealloying mechanism. Once the films are fabricated the ultimate goal becomes their utilization in practice. Therefore, it is highly desired to prepare a large-sized device consisting of a nanofilm,

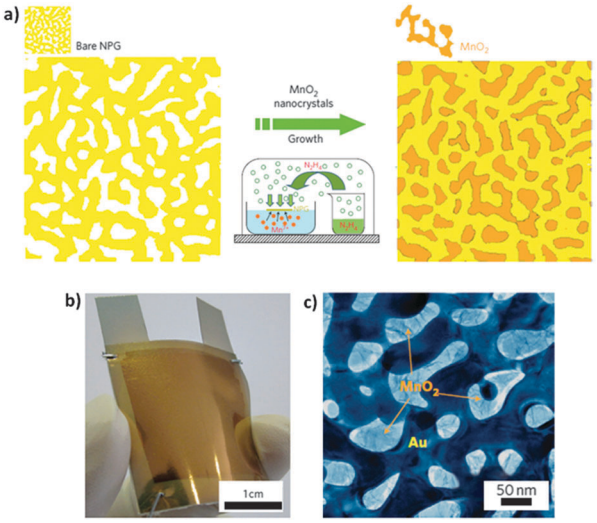

Fig. 11 (a) Schematics showing the fabrication process for nanoporous gold–MnO_2 hybrid materials by directly growing MnO_2 (orange) onto nanoporous gold. (b) Photograph of a nanoporous gold/MnO_2-based supercapacitor. (c) Bright-field TEM image of the nanoporous gold–MnO_2 hybrid with a MnO_2 plating time of 20 min. The hybrid nanostructure can be identified by the contrast between the bright MnO_2 filler and the dark gold skeleton. Reproduced from *Nat. Nanotechnol.*, 2011, **6**, 232. Copyright 2011, Nature.[202]

which can then be directly used. Very recently, Chen *et al.*[202] reported the synthesis of a 100 nm-thick nanoporous gold–MnO_2 composite film *via* a two-step procedure, which included de-alloying $Ag_{65}Au_{35}$ (at%) using HNO_3 to produce conductive nanoporous gold[203,204] followed by plating nanocrystalline MnO_2 into the nanopores (Fig. 11a). Therefore, such large-sized nanoporous gold/MnO_2 films can be utilized as a storage electrode in a simple supercapacitor device architecture (Fig. 11b). The de-alloyed nanoporous gold showed a bicontinuous nanoporous structure (Fig. 11c), which is composed of quasi-periodic gold ligaments and nanopore channels with a characteristic length of 40 nm. And the nanopores are filled with nanocrystalline MnO_2 with a grain size of 5 nm. Further characterizations revealed that the nanocrystalline MnO_2 grows epitaxially on the gold ligament surfaces, forming a chemically bonded metal/oxide interface. The electrical conductivity of the hybrid materials can be significantly improved due to the excellent contact between the nanocrystalline MnO_2 and gold ligaments as well as the detectable charge transfer. Recently, some metal oxides and hybrids with porous hollow structures have been fabricated by using similar methods.[205,206]

4. Photodetecting properties of nanofilm photodetectors

4.1 Nanoparticle based film photodetector

Due to profound quantum and size effects, nanoparticle films become ideal materials for use in photodetectors that rely on a mechanism related to gas adsorption and desorption. A wide range of semiconductor nanoparticles, including ZnO,[207–209]

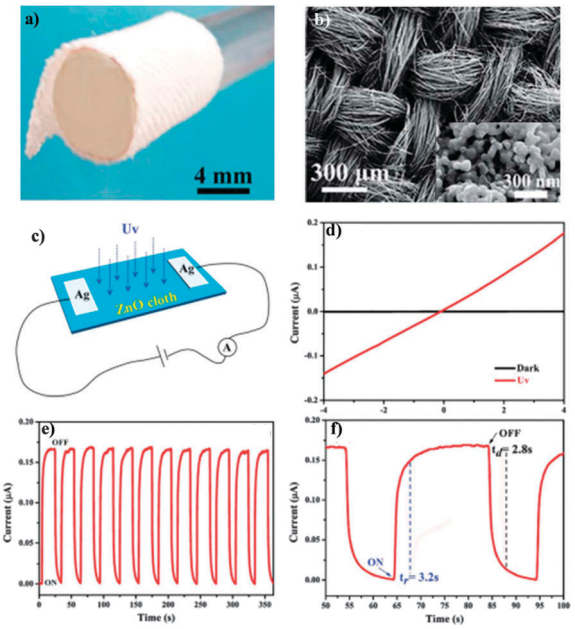

Fig. 12 (a) Photographs of the as-synthesized flexible ZnO cloth. (b) Typical SEM images of the flexible ZnO cloth. The inset is a magnified image. (c) Schematics of the flexible ZnO cloth photodetector device. (d) *I–V* curves showing the dark current and photocurrent of the ZnO device. (e) Photoresponse characteristics of the flexible ZnO cloth photodetectors at a 4 V bias voltage with a 365 nm illuminating UV lamp at a power density of 50 mW cm^{-2}. (f) The rise time (tr) and the decay time (td) of the ZnO cloth device. Reproduced from *J. Mater. Chem.*, 2012, **22**, 9379. Copyright 2012, Royal Society of Chemistry.[207]

Bi_2S_3,[7,8,210] In_2S_3,[12] In_2O_3,[13] PbS[211] and $CuInSe_2$,[212] have been used for the fabrication of nanofilm photodetectors. In this section, we highlight recent progress with respect to ZnO and $CuInSe_2$, and analyze the corresponding photodetector performances.

Shen and coworkers reported the fabrication of a highly flexible, sensitive photodetector built on the flexible nanoparticle-assembled ZnO cloth, which was grown *via* a carbon cloth template hydrothermal method. Fig. 12a shows a photograph of the synthesized product after calcining in air at high temperature, indicating its good flexibility. SEM image of the ZnO product is depicted in Fig. 11b, where one can see that the ZnO product still keeps the textural structure of the carbon cloth template and is woven orderly by many ZnO microfibers (inset of Fig. 12b). Fig. 12c presents the schematic diagram of a flexible ZnO cloth based photodetector. *I–V* characteristics of the flexible ZnO photodetector in the dark and under 365 nm UV light illumination are illustrated in Fig. 12d. At a fixed bias of 4 V, the photocurrent (0.18 μA) is 600 times higher than the dark current (0.3 nA). The I_{Photo}/I_{dark} of the flexible ZnO cloth based photodetector is much higher than that of the previously reported aligned ZnO nanowire based photodetector.[213–215] Fig. 12e reveals the photoresponse switching behavior of the ZnO cloth based photodetector. A photocurrent can be reproducibly switched from the "ON" to the "OFF" state by periodically turning the UV light ON and OFF with a power density of 50 mW cm^{-2} at a low bias voltage of 4 V. Upon illumination, the photocurrent rapidly increased to a stable value of approximately 0.17 μA, and then drastically decreased to its initial level when the light was turned off, indicating the excellent stability and reproducible characteristics of the device. Fig. 12f shows the response time and recovery time of the photodetector, which were found to be around 3.2 s and 2.8 s, respectively. In comparison with other ZnO photodetector devices, the results documented that the ZnO cloth photodetector had exhibited faster photoresponse characteristics.

Wan *et al.* reported the synthesis of high quality $CuInSe_2$ nanocrystals with monodispersed size and uniform hexagonal shape.[212] The TEM images shown in Fig. 13a and b indicate that the as-synthesized nanocrystals are nearly monodispersed. They may easily be self-assembled into 2D arrays because of their uniform shape. A high-performance hybrid photodetector based on a hybrid film of $CuInSe_2$ nanocrystals and poly(3-hexylthiophene) (P3HT) was constructed. A schematic illustration of the device is shown in Fig. 13c. The hybrid device exhibits excellent photoresponse characteristics, as marked in Fig. 13d. With the light irradiation ON and OFF, the current in the device showed two distinct states, a "low" current in the dark and a "high" current under illumination. The switching between these two states was very fast and reversible, allowing the device to act as a high-quality photosensitive switch. In the dark, the current was only 0.15 pA. However, at an incident light density of 7.63 mW cm^{-2} and a bias voltage of 0.4 V, the current could approach 17 pA, giving an ON/OFF switching ratio of >100. When the intensity of the incident light was changed, the photocurrent of the device remarkably changed accordingly (Fig. 13e), which can be attributed to the change in the photon

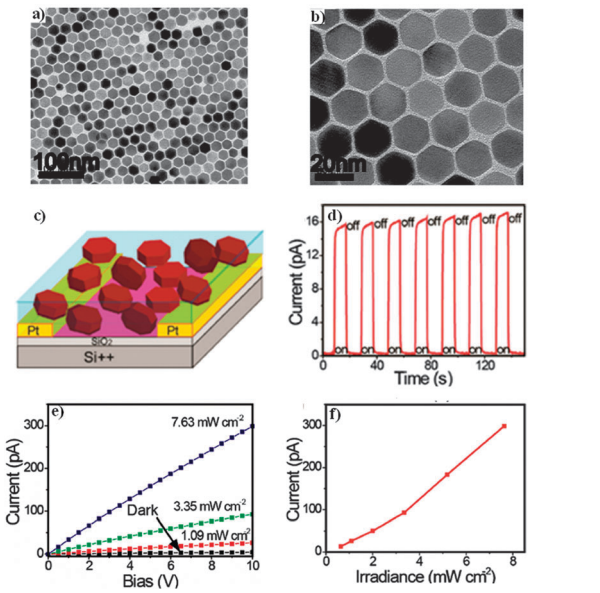

Fig. 13 (a and b) TEM images of as-synthesized $CuInSe_2$ nanocrystals. (c) Schematic illustration of a hybrid device. (d) ON/OFF switching of the hybrid device at an incident light density of 7.63 mW cm^{-2} and a bias voltage of 0.4 V. (e) Dark current and photocurrents at different incident light densities. (f) Photocurrent measured as a function of incident light density at a bias voltage of 10 V. Reproduced from *J. Am. Chem. Soc.*, 2010, **132**, 12218. Copyright 2010, American Chemical Society.[212]

density of the incident light at different light densities. As shown in Fig. 13f, the current of the present hybrid photodetector exhibited a strong dependence on light intensity and demonstrated a power dependence of $I \sim P^{1.34}$, where I is the photocurrent value and P is the light intensity, indicating superior photocurrent capability of the hybrid material. These results prove the promising potential of the hybrid device as a photoswitch and a highly photosensitive detector.

The nanofilms prepared by Rao *et al.*[162] *via* a novel liquid–liquid interface method, consisted of HgSe and $Hg_{0.5}Cd_{0.5}Se$ quantum dos (QDs), which showed superior optoelectronic performances. These were found to be comparable to those of the previously reported high performance QD vis-IR detectors. For example, for the $Hg_{0.5}Cd_{0.5}Se$ QD device, the room-temperature values of the responsivity (R_δ), the external quantum efficiency (EQE) and detectivity ($D^* = (S\Delta f)^{1/2}R_\delta/I_n$, where Δf is the electrical bandwidth (Hz) and I_n the noise current) at 2 V bias and 80 mW A^{-1} intensity are 0.91 A W^{-1}, 72% and 3.3×10^{10} Jones, respectively. This suggested the cost-effectiveness of selenium based IR detectors due to the abundance and lower toxicity of selenium compared to tellurium.

4.2 Nanowire/belt based film photodetector

Benefiting from a large surface-to-volume ratio and a Debye length comparable to a small size, 1D semiconductor nanostructures are considered as the most promising building blocks for photodetectors with superior sensitivity, high quantum efficiency, and fast response. A wide range of semiconductor nanowires/belts, including Ge,[216] CdS,[5] Bi_2S_3,[6] CdSe,[10] Cu_2O,[11] ZnO,[217,218] SnO_2,[43] Zn_2GeO_4, and $In_2Ge_2O_7$,[9] have been used for fabrication of nanofilm photodetectors. In this section, we highlight recent progress with respect to CdSe, ZnO–SnO_2 based film photodetectors, and describe their performance.

Hybrid organic–inorganic P3HT:CdSe nanowire heterojunction photodetectors were first demonstrated on silicon substrates. These exhibited a greatly enhanced photocurrent, a fast response, and a recovery time shorter than 0.1 s. Fig. 14a presents a SEM image of the as-synthesized CdSe nanostructures, revealing the formation of abundant 1-D wire-like materials with a length of hundreds of micrometers. A higher magnification SEM image is shown in the inset of Fig. 14a, where the NWs are seen to have uniform diameters of 100 nm. Fig. 14b depicts the *I–V* curves of the device exposed to white light and under dark conditions. For the hybrid photodetectors, a high photo-excited current of 320 nA was recorded at a low bias of 3.0 V, while only 120 nA was reached for the pure CdSe NWs device. Fig. 14c shows the photocurrent of the hybrid devices during repetitive switching of light illumination, or ON/OFF switching. It should be noted that the hybrid photodetector possessed an outstanding stability. No obvious degradation was observed during many cycles. The high sensitivity and stability of the hybrid devices are promising features for the large-area photodetector applications. As seen, the photocurrent increased and decreased as a response to the ON/OFF states by periodically turning the light on and off with a power of 140 mW cm^{-2} at a bias of 3.0 V. The switching between the two states was very fast and reversible,

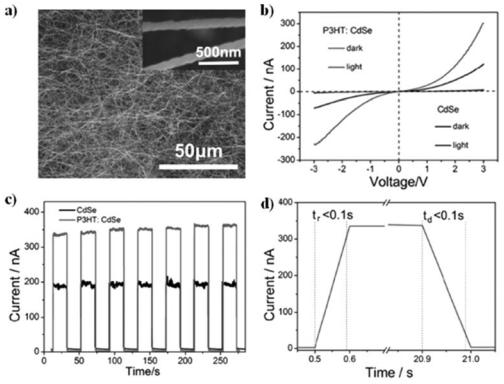

Fig. 14 (a) SEM image of the as-prepared CdSe nanowires. (b) *I–V* characteristics. (c) Reproducible ON/OFF switching. (d) Response time/recovery time of the P3HT:CdSe NW hybrid photodetector on the silicon substrate. Reproduced from *Adv. Funct. Mater.*, 2013, **23**, 1202. Copyright 2013, Wiley-VCH.[10]

allowing the device to act as a high-quality photosensitive switch. For the hybrid photodetectors, the current was only 2.5 nA in the dark. However, at an incident light intensity of 140 mW cm^{-2} and a bias voltage of 3.0 V, the current could approach 350 nA, giving an ON/OFF ratio of 140. The rise time and decay time, defined as the time taken for the initial current to increase to 90% of the peak value, or *vice versa*, are measured to be shorter than 0.1 s, as marked in Fig. 14d.

Recently, we have successfully fabricated a high-performance fully transparent photodetector from the electrospun ZnO–SnO_2 heterojunction nanofiber film.[43] The SEM image shown in Fig. 15a indicates that the diameters of the ZnO–SnO_2 nanofibers range from 100 to 150 nm, and their lengths are several micrometers. The photograph shown in Fig. 15b confirms that a colorful MANA logo beneath the transparent photodetectors can easily be seen, indicating high transparency of the detector. When the device was illuminated by a 300 nm UV light at 0.45 mW cm^{-2}, a drastic current increase, up to 7.9 nA, was detected at an applied voltage of 10.0 V (*i.e.* about 4600 times enhancement compared with a dark current of 1.7 pA). The current also increases when the wavelength of the light sources becomes 250, 280, 320 and 350 nm. The corresponding logarithmic plot (Fig. 15c) clearly evidences that the ratio of photo current to dark current of the pristine nanobelt photodetector is as high as $\sim 5 \times 10^3$ for 300 nm light illumination. We tested the photo currents of the photodetectors irradiated by light of varying intensities. The corresponding dependence of photocurrent on the light power intensity is plotted in Fig. 15d, which can be fitted to a power law, $I \sim P^\theta$. The fitting gives a non-linear behavior with $\theta = 0.51$. The non-unity ($0.5 < \theta < 1$) exponent suggests a complex process of electron–hole generation, recombination, and trapping within a semiconductor.[219] The response of the device under different working atmospheres was also investigated, as illustrated in Fig. 15e. The photocurrent of the device measured in vacuum conditions of 10^{-3} Pa is 149.2 nA, about 18.9 times higher than that in ambient conditions, demonstrating that the photocurrent can be enhanced by decreasing the gas pressure of the environment. Moreover, the dark current is also

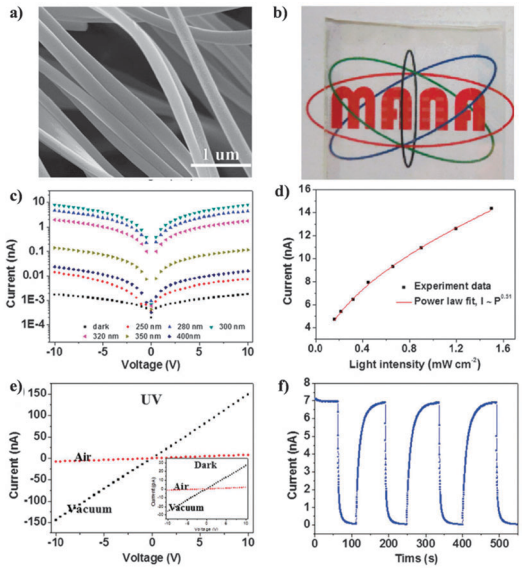

Fig. 15 (a) SEM image of ZnO–SnO_2 nanofibers. (b) Photograph of the final film. (c) Logarithmic plot of *I*–*V* curves of the device illuminated with a light of different wavelengths, and under dark conditions. (d) Photocurrent as a function of light intensity and corresponding fitting curve using the power law under 300 nm light illumination. (e) *I*–*V* curves of the device illuminated with a light of 300 nm wavelength measured under air and vacuum conditions. Inset shows *I*–*V* curves under dark conditions. (f) Time-dependent response of the device measured under air conditions at a bias of 9.0 V under 300 nm light illumination. Reproduced from *Adv. Mater.*, 2013, **25**, 4625. Copyright 2013, Wiley-VCH.[43]

higher in a vacuum, as illustrated in the inset of Fig. 15e. Fig. 15f presents the time dependent photoresponse of the photodetector measured by periodically turning on and off 300 nm light in air. Under closer examination, the rise and decay times of the present detector are measured as 32.2 s and 7.8 s, respectively.

In addition, Rao's group reported graphene or graphene oxide based photodetectors.[220,221] When used as IR detection for an incident wavelength of 1550 nm at 2 V, the responsivity and external quantum efficiency of reduced graphene oxide (RGO) are 4 mA W^{-1} and 0.3%, respectively, whereas for graphene nanoribbons (GNRs) these values are 1000 times higher (1 A W^{-1} and 80%, respectively). They also explored the use of RGO as a candidate for solution processed ultraviolet photodetectors. The photodetecting responsivity was found to be 0.12 A W^{-1} with an external quantum efficiency of 40%. This behaviour can be attributed to the competition between electron trapping by C=O groups and electron photogeneration under light irradiation. All these results clearly suggest that high-selectivity, high sensitivity, and high-speed nanometer-scale photodetectors and photoelectronic switches may be realized by using RGO and GNRs, leading to a strong impact in many future applications of graphene in nanoelectronics.

4.3 Nanoplate-like structures based film photodetector

2D structures often have largely exposed surfaces and specific facets. Such unique structural and surface properties enable them potential application as building blocks for photodetectors.[3,4,222–225]

In this section, we describe recent progress with respect to nanoring and nanosheet film photodetectors, including those made of SnO_2 and $NiCO_2O_4$, and focus on their photodetector performance.

Wu and coworkers constructed a SnO_2 nanonet-based UV photodetector that exhibited an ultrahigh photocurrent and sensitivity, excellent stability, and reproducible characteristics.[3] Fig. 16a shows a typical SEM image of the 2D ordered SnO_2 monolayer nanofilm-based photoresponse device with electrodes separated by about 1.5 μm. Fig. 16b illustrates the *I*–*V* characteristics of the device illuminated with different wavelength lights and under dark conditions. As shown in Fig. 16c, the photocurrent increases gradually as light wavelength is reduced from 600 to 320 nm. The photocurrent under 320 nm light irradiation was 4.1 times of that under the dark current conditions. The difference between the dark-current and the photocurrent reached 285.3 μA. The time-dependent photoresponse of the device is presented in Fig. 16d. This was measured by periodically switching the 320 nm light on and off under air conditions. Upon illumination, the photocurrent increased to a stable value of 2.1 mA and then decreased dramatically to its initial value when the light was turned off.

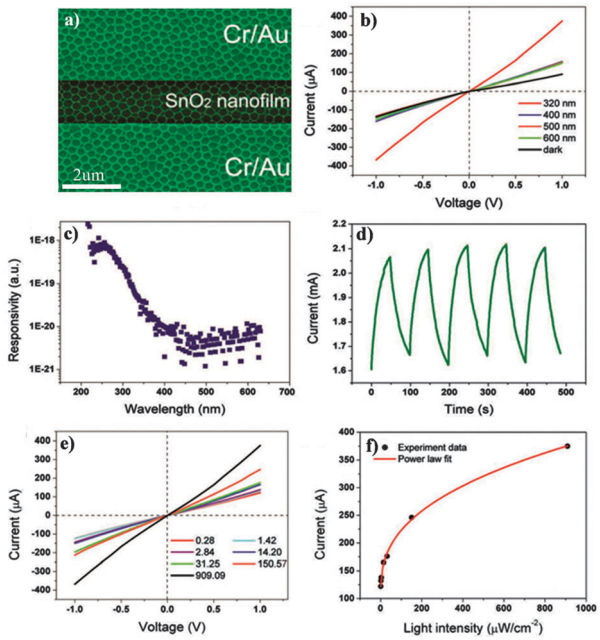

Fig. 16 (a) Typical SEM image of a 2D ordered SnO_2 monolayer nanofilm-based photoresponse device. (b) The *I*–*V* characteristics of the device illuminated with different wavelength lights and under dark conditions. (c) Spectral photoresponse of the device measured at a bias of 5.0 V at diffraction wavelengths ranging from 210 to 630 nm. (d) Time-dependent response of the device measured under air conditions at a bias of 5.0 V, the light power intensity was kept at 0.91 mW cm^{-2} when the UV light was turned on. (e) *I*–*V* characteristics of the device under 320 nm light irradiation with various power intensities. (f) The light-intensity-dependent photocurrent of the device at an excitation wavelength of 320 nm and a bias of 1.0 V, the solid line shows a fitting of power function law $I = 109.78\ 19.00 \times P^{0.39}$, from the experimental data. Reproduced from *Adv. Funct. Mater.*, 2012, **22**, 1229. Copyright 2012, Wiley-VCH.[3]

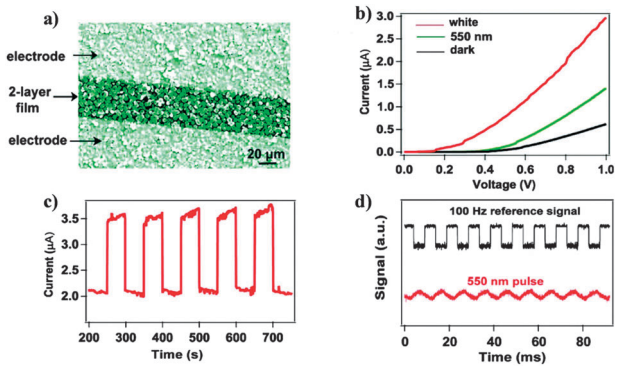

Fig. 17 (a) A representative SEM image of a $NiCo_2O_4$ nanofilm photodetector. (b) The *I–V* characteristics of the $NiCo_2O_4$ nanofilm photodetector illuminated with a green light (550 nm, 26.5 μW cm^{-2}) or a white light (343 mW cm^{-2}). (c) There is reproducible on/off switching upon 550 nm light illumination. (d) A transient response by illuminating $NiCo_2O_4$ film with a 550 nm light pulse chopped at a frequency of 100 Hz. Reproduced from *Adv. Mater.*, 2011, **23**, 1988. Copyright 2011, Wiley-VCH.[4]

This showed the excellent stability and reproducibility of the scheme. To determine the ability of the device to respond to the intensity of the light, we irradiated it with 320 nm light at power intensities ranging from 0.28 to 909.09 μW cm^{-2}. The resulting *I–V* curves are shown in Fig. 16e. The results demonstrated that the photocurrent of the as-fabricated device had been quite dependent on light intensity. The fitting of the dependence of photocurrent to the light intensity gave a power function law, $I \sim P^{0.39}$ (Fig. 16f). By adjusting the intensity of illumination, the current could be reversibly changed 2 to 3 times without damaging the nanofilm.

Fang *et al.* presented the first $NiCo_2O_4$ nanofilm photodetector fabricated by interfacial self-assembly.[4] Hexagonal-shaped $NiCo_2O_4$ platelets were self-assembled at a hexane/water interface to form a high-quality film with preferred orientation. Fig. 17a shows a typical SEM image of the $NiCo_2O_4$ platelet film with a channel width of 50 μm between a pair of electrodes. The *I–V* curves of the nanofilm photodetector with different wavelengths of light and under dark conditions are illustrated in Fig. 17b. An enhancement of current was observed when the device had been illuminated using a light with an energy above the threshold excitation energy, E_g (≈2.10 eV, 589 nm), such as a 550 nm visible light or a white light. At a fixed voltage of 1.0 V, the photocurrent induced by 550 nm light (1.4 μA) and white light (3.0 μA) was about 2.3 and 5.0 times larger than the dark current (0.6 μA), respectively. In the present study, a much higher photocurrent of 3.0 μA was detected at a low applied voltage of 1.0 V when the device had been illuminated with a white light, that is, the photocurrent of the film-based device was significantly enhanced (≈10^3 to 10^6 times) compared with the individual nanostructure-based photodetectors. The high photocurrent of the current film device might be due to a fact that the photocurrent of the device was collected from a large number of $NiCo_2O_4$ platelets rather than from a single platelet. Fig. 17c presents the time-dependent photoresponse of the nanofilm photodetector measured by periodically turning a 550 nm light on and off at a bias of 1.0 V. Upon illumination, the photocurrent rapidly increased to a stable value of 3.5 μA, and then drastically decreased to its initial level when the light was turned off. The detailed response time is shown in Fig. 17d. Both rise and decay times are measured to be within the millisecond time scale. Such fast response is very desirable for the practical application in high-frequency or high-speed devices, such as light wave communications or optoelectronic switches.

4.4 Hollow spheres-based film photodetector

As a unique class of structural materials, hollow spheres, including single-shelled and multi-shelled nanostructures, are important for a wide range of applications. The hollow structures can provide a more efficient way to improve light-harvesting efficiency, due to multi-reflections of light within their interiors. Since the first report on a hollow-sphere nanofilm-based photodetector using ZnO hollow spheres as the building blocks by Wu and co-workers,[2] various hollow spheres, such as those made of Bi_2E_3 (E = S, Se, Te),[226] ZnS,[1,227] SnO_2[42] and ZnO[2,14] have been fabricated and used in photodetectors. In this section, we show recent progress with respect to SnO_2 and ZnO, and focus on their photodetector performances.

In Wu's work,[2] the nanofilm consisted of the ZnO hollow spheres self-assembled at a hexane–water interface. The nanofilm-based constructed device was of a visible-light-blind type and was highly UV-sensitive. There was a drastic increase of current observed when the wavelength of the light source had been changed from 600–400 nm to 350 nm UV light (at 1.32 mW cm^{-2}). This device also showed a high sensitivity, due to a high 4783% of the calculated external quantum efficiency. This superior performance may result from a high light-absorption efficiency of the hollow spheres due to their large active surface. It is also worthy to note that the regarded performance is comparable with that of a ZnS nanostructures-based near-UV-light photodetectors.[22]

Recently, we have constructed a high-quality SnO_2 hollow-sphere nanofilm-based flexible photodetector *via* 'water–oil' interfacial assembling. The photodetector showed high sensitivity, superb stability, and was also able to bear significant external mechanical forces.[42] The typical transmission electron microscopy (TEM) image in Fig. 18a reveals the hollow nature of the product. The configuration of a photoconductive device for the photoresponse measurements is depicted in Fig. 18b. The top inset shows the photograph of the final device on the PET substrate, indicating its flexibility. The bottom inset displays a micrograph of the individual device with a channel width of 40 mm between the two electrodes. Fig. 18c shows the *I–V* curves of the device illuminated with a light of different wavelengths and under dark conditions, respectively. The photoresponsivity only exhibited a very slight change when the wavelengths of the light sources are 600 nm and 500 nm. When the device was illuminated by a 320 nm UV light at 45 mW cm^{-2}, a drastic increase in current, up to 2.2 nA, was detected at an applied voltage of 5.0 V (*i.e.* about 300 times enhancement compared with a dark current of 7.3 pA). We also

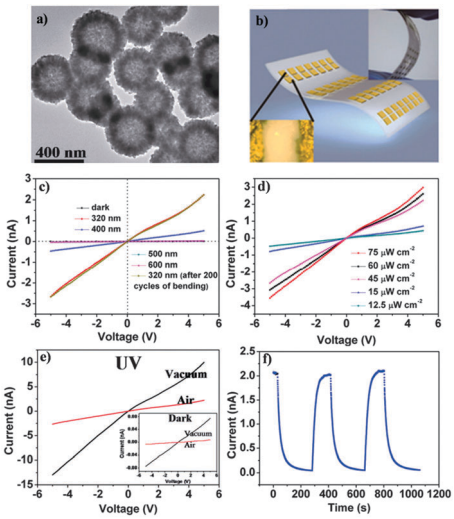

Fig. 18 (a) Typical TEM images of SnO_2 spheres. (b) Schematic illustration of a flexible photodetector. Inset: photograph of the final device (top) and micrograph of a typical device (bottom). (c) *I–V* curves of the device illuminated with a light of different wavelengths, and under dark conditions, and after 200 cycles of bending. (d) *I–V* curves of the device illuminated with a light of 320 nm wavelength with various power intensities. (e) *I–V* curves of the device illuminated with a light of 320 nm wavelength measured under air and vacuum conditions. The inset shows *I–V* curves in the dark. (f) Time-dependent response of the device measured under air conditions at a bias of 5.0 V. Reproduced from *Chem. Commun.*, 2013, **49**, 3739. Copyright 2013, Royal Society of Chemistry.[42]

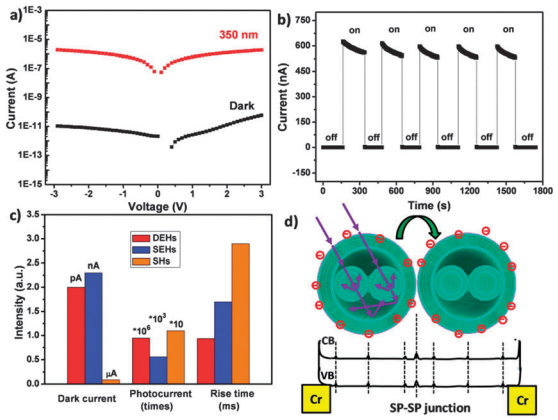

Fig. 19 (a) *I–V* characteristics of a DEHs film photodetector illuminated with a 350 nm light and under dark conditions. (b) The reproducible on/off switching upon 350 nm light illumination. (c) Comparison of the photodetector performance for devices made of ZnO hollow spheres with different morphologies: DEHs, SEHs, and SHs. (d) Schematic illustration of multi-reflections within the DEH structures and the SP–SP junction barriers under the electron transfer within the present unique architecture, showing an increase of the light-harvesting efficiency and lowering of the SP–SP junction barrier height from the light-off to light-on states. Reproduced from *Adv. Mater.*, 2012, **24**, 3421. Copyright 2012, Wiley-VCH.[14]

investigated the mechanical stability of the device by its repeatable bending on the PET substrate. After bending for 200 times, the *I–V* curve was nearly unchanged when compared with the corresponding initial *I–V* curve (without bending) under 320 nm UV light. These results indicate that the present flexible ultraviolet photodetector is able to decently bear external mechanical forces. Fig. 18d displays the *I–V* curves of photodetectors irradiated by 320 nm light of varying intensities. The photocurrent increases with the light intensity, consistent with the fact that the charge carrier photogeneration efficiency is proportional to the absorbed photon flux. The responses of the device under different working atmospheres were also investigated, as illustrated in Fig. 18e. The photocurrent of the device measured under vacuum conditions of 0.1 Pa is about 4.3 times higher than that under ambient conditions, demonstrating that the photocurrent can be enhanced by decreasing the gas pressure of the environment. Moreover, the dark current is also higher under vacuum conditions. Fig. 18f displays the time dependent photoresponse of the photodetector measured by periodically turning a 320 nm light on and off under air conditions. Upon illumination, the photocurrent increased to a stable value of 2.2 nA, and then dramatically decreased to its initial value as the light was turned off, thereby showing excellent stability and reproducibility of the device.

We also fabricated film photodetector devices composed of ZnO hollow spheres with double-yolk egg structures (DEHs) and measured their performances.[14] Fig. 19a depicts *I–V* curves of the DEH device, measured in dark conditions and under 350 nm-light illumination (1.32 mW cm^{-2}), respectively. Compared with a dark current, the photocurrent increases by nearly a million times, whereas this value for single-yolk-egg structures (SEHs) and single-shelled hollow spheres (SHs) is only about 565 and 11 times (Fig. 19c), respectively. The responsivity at 350 nm is as high as 35.9 A W^{-1}, corresponding to a quantum efficiency of 1.27×10^4%. These values are much higher than those of SEHs and SHs. This clearly indicates the ultimately high sensitivity of the DEH photodetector. In addition, such a photodetector has a very fast response time, and excellent stability and repeatability, which were measured by periodic turning of a 350 nm-light on and off at a bias voltage of 3.0 V (Fig. 19b). Both rise and decay times were found to be ~960 μs. These figures are much shorter than those for SEH- and SH-based schemes. The present superior performance of DEHs-based detectors may be attributed to the following reasons. Firstly, the hollow double-yolk egg structures can provide a more efficient way to enhance light-harvesting efficiency (Fig. 19d). Such assumption looks reasonable since such structures possess an increased active surface area, and enable multiple light reflection and scattering between one outer spherical shell and the two interior shells compared with single-shelled, and single-yolk egg hollow spheres (Fig. 19d). Furthermore, it is believed that the shells of different sizes inside a microsphere can also scatter the incident light of different wavelengths within the UV range.[208] Therefore, the "hollow yolk" in the DEHs nanostructures allows the photo-carrier generation dominated by the bulk rather than the surface absorption–desorption process.[228] Secondly, the special conducting mechanism comes into effect. As illustrated in Fig. 19d, the increased carrier density in a DEH film upon illumination lowers the effective barrier height, leading to the

easier carriers tunnelling and carrier transport and, thus, to a significant enhancement in conductivity.[229] The light-induced barrier height modulation is much faster than the surface dominated oxygen-diffusion process (the latter determines the individual nanostructure device performance).[230] These two reasons provide the high photoresponsivity without loss of the response speed. Therefore, either the quantum efficiency or the response speed for the present DEHs network device is much better than these parameters for the individual nanostructure-based ZnO devices, SEHs, and SHs.

5. Summary and outlook

In this review, we have outlined an important topic pertinent to solution-processed nanofilm photodetectors, especially highlighting the recent advances in the wet-chemical fabrication of nanofilms as building blocks and the construction of nanofilm-based photodetectors. In the initial section, we have described in detail the direct chemical syntheses and newly devolved liquid strategies for making nanofilms. Especially, the key points of these approaches that influence the formation of various building blocks have been summarized. The methods for assembly and transfer techniques of these building units into integrated (free-standing) nanofilms have also been discussed. In the following application section, we present some recent progress on the construction of nanofilm-based photodetectors. The photodetector performances of variously assembled nanofilms, including nanoparticle-, nanowire/belt-, nanoplate-like structures- and hollow spheres-based ones, have been analyzed.

Table 1 summarizes the characterizations of nanofilms made by various solution-processed methods. Each method has its own advantages and disadvantages. For example, in terms of nanofilm quality, oil–water interfacial self-assembly, liquid–liquid interface strategy, and dealloying method are generally better than other approaches. That is because highly densely packed building blocks, such as monodispersed nanostructures and even bicontinuous nanoporous scaffolds exist in as-made nanofilms. In contrast, the low area coverage ratio and abundant congeries of nanomaterials are usually found in the layer-by-layer assembly and spin-coating methods. As far as applicability and controllability are concerned, self-assembly, vacuum filtration, and roll-based production seem to be more attractive. Spin-coating requires uniform-size nanoparticles, electrospinning needs high-voltage instruments, and M-ink film is not applicable for non-magnetic nanoparticles.

Table 2 presents a summary of several selected nanofilm photodetector performances. It is relatively hard to simply compare their performances (since they have been made using various methods), in fact the performances are usually dependent on many factors including processing procedures and functional groups. The photodetecting properties also depend on the device fabrication details such as the metal electrodes type, electrode gap, and post processing. However, nanofilm quality should be one of the main parameters. Depending on this, as-measured photodetector properties can partly reflect the film quality. As observed in Table 2, solution-processed assembly strategies seem to be decently better because of the peculiar more intimate contacts and nearly monolayer features. Another advantage of these methods is that one can use various building blocks, such as various semiconducting nanowires, nanotubes and nanorods to fabricate the photodetector devices. Therefore, one can clarify on the morphology dependent properties of these devices and further expect the enhancement in the device performance. Regarding flexible nanodevices, some strategies including a roll-based production may be a better choice with respect to the device performance optimization. Above all, the design of nanofilms with special microstructural characteristics has led to the establishment of structure-performance correlations toward desired electronic/photonic structures, thereby opening the door for applying these nanofilms in photodetector applications. Although some significant developments have been made, more efforts still need to be done to meet the growing demands of this rapidly developing field.

1. It is believed that the following aspects shall be paid more attention to in future research:

(a) Scale-up production of nanofilms. The researchers' ability to employ straightforward techniques to nanofilm

Table 1 Comparison of nanofilms prepared by various solution-processing methods (Y represents yes, N stays for no)

Building blocks-built nanofilms	Methods	Operation	Flexibility	Transparency	Cost	Scaling-up	Ref.
ZnO hollow spheres-based film	Spin coating	Easy	N	N	Moderate	Possible	14
IZO:F TFT on PEN film	Spin coating	Easy	Y	Y	—	Possible	108
SWCNT network film	Spin coating	Easy	Y	Y	—	Possible	109
Nano-trough network	Electro-spinning	Multi-steps	Y	Y	Low	Y	140
1D porous carbon micro-fibers-based film	Electro-spinning	Easy	Y	N	Low	Possible	143
$Co(OH)_2$ platelet mono-layer film	Oil–water self-assembly	Multi-steps	—	N	Moderate	Possible	155
$NiCo_2O_4$ platelet mono-layer film	Oil–water self-assembly	Multi-steps	—	N	Moderate	Possible	4
ZnO hollow sphere	Oil–water self-assembly	Multi-steps	—	N	Moderate	Possible	2
HgSe	Liquid–liquid interface strategy	One step	—	N	Low	Possible	162
M-ink film	"Magnetic ink"	Multi-steps	Y	N	—	Y	178
PbS nano-sheets	Oriented attachment strategy	One step	—	—	—	Possible	180
Graphene film	A dry-transfer process	Multi-steps	Y	Y	Low	Y	128
BN, MoS_2, and WS_2 free-standing films	Vacuum filtration or spraying	Easy	Y	N	Low	Y	190
LDH-based ultrathin films	LBL	Multi-steps	Y	Y	—	Y	184
Nanoporous films	Dealloying method	Easy	Y	N	High	Y	202
Graphene films	A roll-based production	Multi-steps	Y	Y	Low	Y	130
Graphene films	Liquid electrolyte-mediated method	Easy	Y	N	Low	Y	201

Table 2 Key nanofilm photodetector parameters reported recently

Film photo-detectors	Methods	Light of detection	Bias/ V	Dark-current or conductance	Photo-current or conductance	Rise time	Decay time	Ref.
ZnO cloth	Template-assisted hydro-thermal methods	365 nm	4	0.3 nA	0.2 μA	3.2 s	2.8 s	207
$CuInSe_2$ nanocrystal	Spin coating	White light	0.4	0.15 pA	17 pA	—	—	212
Ge nanowire	Spraying	White light	5	—	0.4 μA	<10 ms	<10 ms	216
CdS nanowire	Directed assembly	White light		0.078 nS	2.4 nS	0.8 ms	240 ms	5
P3HT:CdSe nanowire	Spin-coating	White light	3	2.5 nA	350 nA	<0.1 s	<0.1s	10
ZnO–SnO_2 nanofibers	Electro-spinning	300 nm	10	1.7 pA	7.9 nA	32.2 s	7.8 s	43
SnO_2 nanonet	Oil–water self-assembly	320 nm	1	89.9 μA	375.2 μA	—	—	3
$NiCo_2O_4$ platelet	Oil–water self-assembly	550 nm	1	0.6 μA	1.4 μA	~ms	~ms	4
ZnS hollow sphere	Oil–water self-assembly	320 nm	8	<3 pA	17.9 pA	~100 s	~100 s	207
ZnS–ZnO bi-layer film	Oil–water self-assembly	370 nm	5	15.1 nA	18 μA	~50 s	~50 s	1
ZnO hollow sphere	Oil–water self-assembly	350 nm	5	50 nA	2.6 μA	<5 ms	<5 ms	2
ZnO hollow sphere	Spin-coating	350 nm	3	2 pA	1.9 μA	~946 μs	~960 μs	14
SnO_2 hollow sphere	Oil–water self-assembly	320 nm	5	7.3 pA	2.2 nA	—	—	42

making implies a bright future in this area. However, there remains a number of substantial challenges. There are many requirements (Table 1) in order to realize this target, such as easy operation and low cost. Although some new methods mentioned above have great promise, they also have a number of limitations at present. For example, the yield of building blocks, especially monolayer nanosheets, generally does not exceed a few tens of percent, which is far too low for many applications (Fig. 20). As such, new approaches will be necessary to develop, monitor and increase the yield. Furthermore, the required time for preparation of building blocks and nanofilms must be reduced. Moreover, a goal of more than a dozen kilograms per day throughput should be targeted and realized, because the ultimate goal is an industrial scale production. Just as Table 2 and Fig. 19 show, some great progress has been made in the area of large-scale preparation of nanofilms. However, the required production yield needs an additional effort.

(b) New strategies for flexible and transparent nanofilms. Nowadays, the flexible and transparent film devices have demonstrated exciting perspective. And it is believed that there will be a huge market due to the exceptionally rising demand. However, efforts to make transparent conducting nanofilms have been hampered by the lack of efficient methods for the synthesis and transfer at the scale and quality required for applications. Therefore, it is still highly desired to develop new and simple approaches for the fabrication of high-quality special nanofilms (Table 1).[130,201] Fig. 20e and f show a good example of scale-up production of flexible and transparent nanofilms. It can be seen that an assembled graphene/PET touch panel possesses outstanding flexibility, and can be easily connected to a computer with control software. In the regarded report, the roll-to-roll production and wet-chemical doping of monolayer 30-inch graphene films grown onto flexible copper substrates[130] could simultaneously be realized. In addition, there are no general and versatile methods to produce assembled nanofilms. For example, to date, liquid exfoliation has produced graphenes, h-BN, a range of metal oxides and hydroxides, a number of clays, and other exfoliated nanosheets. However, there is a galaxy of other materials offering a rich set of distinct features that have not yet been exfoliated but should be amenable to the methods described above.

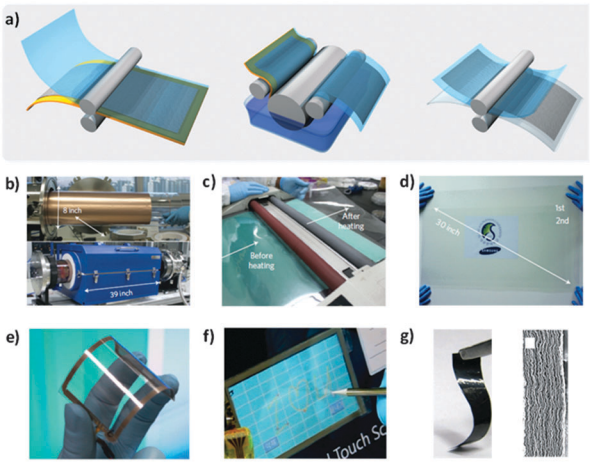

Fig. 20 (a) Schematics of the roll-based production of graphene films grown on a copper foil. The process includes adhesion of polymer supports, copper etching (rinsing) and dry transfer-printing on a target substrate. A wet-chemical doping can be carried out using a set-up similar to that used for etching. (b–g) Photographs of the roll-based production of graphene films: (b) copper foil wrapped around a 7.5-inch quartz tube to be inserted into an 8-inch quartz reactor. The lower image shows the stage in which the copper foil reacts with CH_4 and H_2 gases at high temperatures. (c) Roll-to-roll transfer of graphene films from a thermal release tape to a PET film at 120 °C. (d) A transparent ultralarge-area graphene film transferred on a 35-inch PET sheet. (e) An assembled graphene/PET touch panel showing outstanding flexibility. (f) A graphene-based touch-screen panel connected to a computer with control software. Reproduced from *Nat. Nanotechnol.*, 2010, **5**, 574. Copyright 2010, Nature.[130] (g) Characterization of liquid electrolyte-mediated CCG (EM-CCG) films: a photograph (left) showing the flexibility of the film, and SEM image of cross sections of the obtained EM-CCG films containing 27.2 vol% of H_2SO_4. Reproduced from *Science*, 2013, **341**, 534. Copyright 2013, AAAS.[201]

(c) The used strategies for nanofilm production should be used to not only fabricate photodetectors, but also to design them within other nanodevices, such as nanofilm-based field-emission transistors (FETs), solar cells, gas sensors, flat panel displays and light emitting diodes (LEDs).

2. High-performance photodetectors with a low cost and high efficiency have been obtained based on the as-assembled nanofilms. However, it is still an incubation stage with respect to the device construction strategy. Herein, the following aspects related to photodetector applications should be emphasized:

(a) Since many building blocks with different shapes have been used for construction of nanofilm-based photodetectors, one should clarify on the morphology dependent properties of these devices and on how to further enhance the device performance *via* a control of building units (Table 2). In addition, multi-functional nanodevices should be considered. Therefore, a large variety of functionalities must be realized, if other functional nanodevices (*e.g.* solar cells) can be integrated into a nanodevice in addition to a photodetector.

(b) Nanofilms with many compositions and complex structures, such as hybrid, heterostructures, and multilayers should be prepared. Therefore, the dependence of the performance on the layer-number and compositions should be studied. Also one can investigate how heterostructures of the hetero-assembled films affect the behavior of the as-constructed photodetectors in order to finally optimize the performance.

In summary, one shall pay more attention to the synthetic strategies toward nanofilm fabrication and their assembling as versatile building blocks. This could guide one toward the optimized design, fundamental applications and theoretical analyses. Furthermore, more attention should be drawn to the assembly and transfer techniques of free-standing building units into integrated films and a design of high-performance low-cost, high-performance photodetector devices. We do hope that a reader can acquire more knowledge and the necessary background in this field while reading this review. And even more importantly, we do expect that this review can stimulate young researchers to search and find new and interesting topics in this burgeoning area.

Acknowledgements

This work was supported by the International Center for Young Scientists (ICYS) of the International Center for Materials Nanoarchitectonics (WPI-MANA) tenable at the National Institute for Materials Science (NIMS). We also thank Prof. Zhai's kind discussion in the preparation process of this paper and acknowledge the support of the National 1000 Talents Program of China tenable in HUST and the National Nature Science Foundation of China (No. 21322106).

References

1 L. F. Hu, M. Chen, W. Z. Shan, T. R. Zhan, M. Y. Liao, X. S. Fang, X. H. Hu and L. M. Wu, *Adv. Mater.*, 2012, **24**, 5872.
2 M. Chen, L. F. Hu, J. X. Xu, M. Y. Liao, L. M. Wu and X. S. Fang, *Small*, 2011, **7**, 2449.
3 H. Chen, L. F. Hu, X. S. Fang and L. M. Wu, *Adv. Funct. Mater.*, 2012, **22**, 1229.
4 L. F. Hu, L. M. Wu, M. Y. Liao and X. S. Fang, *Adv. Mater.*, 2011, **23**, 1988.
5 K. Heo, H. Lee, Y. Park, J. Park, H. J. Lim, D. Yoon, C. Lee, M. Kim, H. Cheong, J. Park, J. Jian and S. Hong, *J. Mater. Chem.*, 2012, **22**, 2173.
6 H. Bao, C. M. Li, X. Cui, Q. Song, H. Yang and J. Guo, *Nanotechnology*, 2008, **19**, 335302.
7 A. A. Tahir, M. A. Ehsan, M. Mazhar, K. G. U. Wijayantha, M. Zeller and A. D. Hunter, *Chem. Mater.*, 2010, **22**, 5084.
8 F. A. Liu, Y. C. Yang, J. Liu, W. Huang and Z. L. Li, *J. Electroanal. Chem.*, 2012, **665**, 58.
9 Z. Liu, H. T. Huang, B. Liang, X. F. Wang, Z. R. Wang, D. Chen and G. Z. Shen, *Opt. Express*, 2012, **20**, 2982.
10 X. F. Wang, W. F. Song, B. Liu, G. Chen, D. Chen, C. W. Zhou and G. Z. Shen, *Adv. Funct. Mater.*, 2013, **23**, 1202.
11 S. Sahoo, S. Husale, B. Colwill, T. M. Lu, S. Nayak and P. M. Ajayan, *ACS Nano*, 2009, **3**, 3935.
12 J. Tang, G. Konstantatos, S. Hinds, S. Myrskog and A. G. Pattantyus-Abraham, *ACS Nano*, 2009, **3**, 331.
13 D. L. Shao, L. Q. Qin and S. Sawyer, *Appl. Surf. Sci.*, 2012, **261**, 123.
14 X. Wang, M. Liao, Y. Zhong, J. Y. Zheng, W. Tian, T. Zhai, C. Zhi, Y. Ma, J. Yao, Y. Bando and D. Golberg, *Adv. Mater.*, 2012, **24**, 3421.
15 H. Li, X. Wang, J. Xu, Q. Zhang, Y. Ma, Y. Bando, D. Golberg and T. Zhai, *Adv. Mater.*, 2013, **25**, 3017.
16 L. Li, H. Lu, Z. Y. Yang, L. M. Tong, Y. Bando and D. Golberg, *Adv. Mater.*, 2012, **25**, 1109.
17 T. Y. Zhai, H. M. Liu, H. Q. Li, X. S. Fang, M. Y. Liao, L. Li, H. S. Zhou, Y. Koide, Y. Bando and D. Golberg, *Adv. Mater.*, 2010, **22**, 2547.
18 L. Li, P. S. Lee, C. Y. Yan, T. Y. Zhai, X. S. Fang, M. Y. Liao, Y. Koide, Y. Bando and D. Golberg, *Adv. Mater.*, 2010, **22**, 5145.
19 L. Li, P. C. Wu, X. S. Fang, T. Y. Zhai, L. Dai, M. Y. Liao, Y. Koide, H. Q. Wang, Y. Bando and D. Golberg, *Adv. Mater.*, 2010, **22**, 3161.
20 T. Y. Zhai, M. F. Ye, L. Li, X. S. Fang, M. Y. Liao, Y. F. Li, Y. Koide, Y. Bando and D. Golberg, *Adv. Mater.*, 2010, **22**, 4530.
21 L. Li, X. S. Fang, T. Y. Zhai, M. Y. Liao, U. K. Gautam, X. C. Wu, Y. Koide, Y. Bando and D. Golberg, *Adv. Mater.*, 2010, **22**, 4151.
22 X. S. Fang, Y. Bando, M. Y. Liao, U. K. Gautam, C. Y. Zhi, B. Dierre, B. D. Liu, T. Y. Zhai, T. Sekiguchi, Y. Koide and D. Golberg, *Adv. Mater.*, 2009, **21**, 2034.
23 X. S. Fang, S. L. Xiong, T. Y. Zhai, Y. Bando, M. Y. Liao, U. K. Gautam, Y. Koide, X. G. Zhang, Y. T. Qian and D. Golberg, *Adv. Mater.*, 2009, **21**, 5016.
24 K. Sun, Y. JIng, N. Park, C. Li, Y. Bando and D. Wang, *J. Am. Chem. Soc.*, 2010, **132**, 15465.
25 X. S. Fang, Y. Bando, U. Gautam, T. Zhai, H. Zeng, X. Xu, M. Liao and D. Golberg, *Crit. Rev. Solid State Mater. Sci.*, 2009, **34**, 190.
26 X. S. Fang, Y. Bando, M. Y. Liao, T. Y. Zhai, U. K. Gautam, L. Li, Y. Koide and D. Golberg, *Adv. Funct. Mater.*, 2010, **20**, 500.

27 X. S. Fang, L. Hu, K. Huo, B. Gao, L. Zhao, M. Liao, P. Chu, Y. Bando and D. Golberg, *Adv. Funct. Mater.*, 2011, **21**, 3907.
28 T. Y. Zhai, L. Li, X. Wang, X. Fang, Y. Bando and D. Golberg, *Adv. Funct. Mater.*, 2009, **20**, 4233.
29 T. Y. Zhai, X. S. Fang, M. Y. Liao, X. J. Xu, L. Li, B. D. Liu, Y. Koide, Y. Ma, J. N. Yao, Y. Bando and D. Golberg, *ACS Nano*, 2010, **4**, 1596.
30 X. S. Fang, T. Y. Zhai, L. Li, L. M. Wu, Y. Bando and D. Golberg, *Prog. Mater. Sci.*, 2011, **56**, 175.
31 T. Y. Zhai, L. Li, Y. Ma, M. Liao, X. Wang, J. Yao, Y. Bando and D. Golberg, *Chem. Soc. Rev.*, 2011, **40**, 2986.
32 X. Wang, W. Tian, T. Zhai, C. Zhi, Y. Bando and D. Golberg, *J. Mater. Chem.*, 2012, **22**, 23310.
33 W. Tian, C. Y. Zhi, T. Y. Zhai, S. M. Chen, X. Wang, M. Y. Liao, D. Golberg and Y. Bando, *J. Mater. Chem.*, 2012, **22**, 17984.
34 T. Y. Zhai, Y. Ma, L. Li, X. S. Fang, M. Y. Liao, Y. Koide, J. N. Yao, Y. Bando and D. Golberg, *J. Mater. Chem.*, 2010, **20**, 6630.
35 J. Li, H. Zhong, H. Liu, T. Zhai, X. Wang, M. Liao, Y. Bando, R. Liu and B. Zou, *J. Mater. Chem.*, 2012, **22**, 17813.
36 L. Li, Y. Zhang, X. S. Fang, T. Y. Zhai, M. Y. Liao, X. Sun, Y. Bando and D. Golberg, *J. Mater. Chem.*, 2011, **21**, 6525.
37 W. Tian, C. Zhi, T. Zhai, X. Wang, M. Liao, S. Li, S. Chen, D. Golberg and Y. Bando, *Nanoscale*, 2012, **4**, 6318.
38 L. Li, E. Auer, M. Y. Liao, X. S. Fang, T. Y. Zhai, U. K. Gautam, A. Lugstein, Y. Koide, Y. Bando and D. Golberg, *Nanoscale*, 2011, **3**, 1120.
39 C. Li, Y. Bando, M. Y. Liao, Y. Koide and D. Golberg, *Appl. Phys. Lett.*, 2010, **97**, 161102.
40 B. D. Liu, Y. Bando, M. Y. Liao, C. C. Tang, M. Mitome and D. Golberg, *Cryst. Growth Des.*, 2009, **9**, 2790.
41 L. Li, Y. Zhang, X. S. Fang, T. Y. Zhai, M. Y. Liao, H. Q. Wang, G. H. Li, Y. Koide, Y. Bando and D. Golberg, *Nanotechnology*, 2011, **22**, 165704.
42 W. Tian, C. Zhang, T. Zhai, S. Li, X. Wang, M. Liao, K. Tsukagoshi, D. Golberg and Y. Bando, *Chem. Commun.*, 2013, **49**, 3739.
43 W. Tian, T. Y. Zhai, C. Zhang, S. L. Li, X. Wang, F. Liu, D. Q. Liu, X. K. Cai, K. Tsukagoshi, D. Golberg and Y. Bando, *Adv. Mater.*, 2013, **25**, 4625.
44 T. E. Vandervelde and S. Krishna, *J. Nanosci. Nanotechnol.*, 2010, **10**, 1450.
45 P. F. Xu, H. M. Ji, T. Yang, B. Xu, W. Q. Ma and Z. G. Wang, *J. Nanosci. Nanotechnol.*, 2011, **11**, 9345.
46 A. D. Stiff-Roberts, *Opto-Electron. Rev.*, 2008, **16**, 458.
47 P. Martyniuk and A. Rogalski, *Prog. Quantum Electron.*, 2008, **32**, 89.
48 K. F. Brennan and J. Haralson, *Superlattices Microstruct.*, 2000, **28**, 77.
49 S. D. Gunapala, S. V. Bandara, J. K. Liu, E. M. Luong, S. B. Rafol, J. M. Mumolo, D. Z. Ting, J. J. Bock, M. Ressler, M. Werner, P. LeVan, R. Chehayeb, C. Kukkonen, M. Levy, P. LeVan and M. Fauci, *Sens. Mater.*, 2000, **12**, 327.
50 J. L. Pan and C. G. Fonstad, *Mater. Sci. Eng., R*, 2000, **28**, 65.
51 V. G. Erofeichev, *J. Opt. Technol.*, 2000, **67**, 3.
52 C. Soci, A. Zhang, X. Y. Bao, H. Kim, Y. Lo and D. L. Wang, *J. Nanosci. Nanotechnol.*, 2010, **10**, 1430.
53 C. Y. Yan and P. S. Lee, *Sci. Technol. Adv. Mater.*, 2012, **4**, 241.
54 A. V. Barve, S. J. Lee, S. K. Noh and S. Krishna, *Laser Photonics Rev.*, 2010, **4**, 738.
55 T. Y. Zhai, X. S. Fang, M. Y. Liao, X. J. Xu, H. B. Zeng, Y. Bando and D. Golberg, *Sensors*, 2009, **9**, 6504.
56 J. Michel, J. F. Liu and L. C. Kimerling, *Nat. Photonics*, 2010, **4**, 527.
57 K. W. Liu, M. Sakurai and M. Aono, *Sensors*, 2010, **10**, 8604.
58 P. Peumans, A. Yakimov and S. R. Forrest, *J. Appl. Phys.*, 2003, **93**, 3693.
59 M. Casalino, G. Coppola, M. Iodice, I. Rendina and L. Sirleto, *Sensors*, 2010, **10**, 10571.
60 A. Beling and J. C. Campbell, *J. Lightwave Technol.*, 2009, **27**, 343.
61 E. Monroy, F. Omnes and F. Calle, *Semicond. Sci. Technol.*, 2003, **18**, R33.
62 A. F. Buzulutskov, *Physics of Particles and Nuclei*, 2008, **39**, 424.
63 C. H. Lin and C. W. Liu, *Sensors*, 2010, **10**, 8797.
64 S. H. Hsu, *Sensors*, 2010, **10**, 10863.
65 S. C. Kong and Y. W. Choi, *J. Comput. Theor. Nanosci.*, 2009, **6**, 2380.
66 A. Rogalski, J. Antoszewski and L. Farane, *J. Appl. Phys.*, 2009, **105**, 091101.
67 S. Feruglio, G. N. Lu, P. Garda and G. Vasilescu, *Sensors*, 2008, **8**, 6566.
68 M. Razeghi and A. Rogalski, *J. Appl. Phys.*, 1996, **79**, 7433.
69 J. D. Prades, F. Hernandez-Ramirez, R. Jimenez-Diaz, M. Manzanares, T. Cirera, A. Romano-Rodriguez and J. R. Morante, *Nanotechnology*, 2008, **19**, 465501.
70 J. S. Jie, W. J. Zhang, Y. Jiang, X. M. Meng, Y. Q. Li and S. T. Lee, *Nano Lett.*, 2006, **6**, 1887.
71 C. Soci, A. Zhang, B. Xiang, S. A. Dayeh, D. P. R. Aplin, J. Park, X. Y. Bao, Y. H. Lo and D. Wang, *Nano Lett.*, 2007, **7**, 1003.
72 Y. N. Xia and G. M. Whitesides, *Annu. Rev. Mater. Sci.*, 1998, **28**, 153.
73 A. Tao, P. Sinsermsuksakul and P. Yang, *Nat. Nanotechnol.*, 2007, **2**, 435.
74 Z. W. Mao, H. L. Xu and D. Y. Wang, *Adv. Funct. Mater.*, 2010, **20**, 1053.
75 Y.-K. Park, S.-H. Yoo and S. Park, *Langmuir*, 2007, **23**, 10505.
76 I. A. Aksay, M. Trau, S. Manne, I. Honma, N. Yao, L. Zhou, P. Fenter, P. M. Eisenberger and S. M. Gruner, *Science*, 1996, **273**, 892.
77 B. L. Smith, T. E. Sch€affer, M. Viani, J. B. Thompson, N. A. Frederick, J. Kindt, A. Belcher, G. D. Stucky, D. E. Morse and P. K. Hansma, *Nature*, 1999, **399**, 761.
78 J. H. Lee, S. W. Rhee and D. Y. Jung, *Chem. Commun.*, 2003, 2740.
79 J. H. Lee, S. W. Rhee and D. Y. Jung, *Chem. Mater.*, 2006, **18**, 4740.

80 P. Podsiadlo, A. K. Kaushik, E. M. Arruda, A. M. Waas, B. S. Shim, J. D. Xu, H. Nandivada, B. G. Pumplin, J. Lahann, A. Ramamoorthy and N. A. Kotov, *Science*, 2007, **318**, 80.
81 L. J. Bonderer, A. R. Studart and L. J. Gauckler, *Science*, 2008, **319**, 1069.
82 F. M. van der Kooij, K. Kassapidou and H. N. W. Lekkerkerker, *Nature*, 2000, **406**, 868.
83 D. van der Beek, P. B. Radstake, A. V. Petukhov and H. N. W. Lekkerkerker, *Langmuir*, 2007, **23**, 11343.
84 T.-H. Lin, W.-H. Huang, I.-K. Jun and P. Jiang, *Chem. Mater.*, 2009, **21**, 2039.
85 L. Hu, R. Ma, T. C. Ozawa, F. Geng, N. Iyi and T. Sasaki, *Chem. Commun.*, 2008, 4897.
86 L. Hu, R. Ma, T. C. Ozawa and T. Sasaki, *Angew. Chem., Int. Ed.*, 2009, **48**, 3846.
87 http://large.stanford.edu/courses/2007/ph210/hellstrom1/.
88 J. H. Burroughs, D. D. C. Bradley, A. R. Brown, R. N. Mark, K. Mackay, R. H. Frined, P. L. Burns and A. B. Holmes, *Nature*, 1990, **347**, 539.
89 M. Madou, *The science of miniaturization*, CRC Press, 2002.
90 J. H. Lai, *Polym. Eng. Sci.*, 1979, **19**, 1117.
91 W. J. Daughton and F. L. Givens, *J. Electrochem. Soc.*, 1982, **129**, 173.
92 D. Meyerhofer, *J. Appl. Phys.*, 1978, **49**, 3993.
93 D. E. Bornside, C. W. Macosko and L. E. Scriven, *J. Electrochem. Soc.*, 1991, **138**, 317.
94 D. E. Bornside, C. W. Macosko and L. E. Scriven, *Phys. Fluids A*, 1991, **3**, 733.
95 J. A. Moriarty, L. W. Schwartz and E. O. Tuck, *J. Appl. Phys.*, 1989, **66**, 5185.
96 D. Wang and H. Möhwald, *Adv. Mater.*, 2004, **16**, 244.
97 R. Biswas, M. M. Sigalas, G. Subramania and K. M. Ho, *Phys. Rev. B: Condens. Matter*, 1998, **57**, 3701.
98 A. Kirihara, K. Uchida, Y. Kajiwara, M. Ishida, Y. Nakamural, T. Manako, E. Saitoh and S. Yorozu, *Nat. Mater.*, 2012, **11**, 686.
99 K. Uchida, S. Takahashi, K. Harii, J. Ieda, W. Koshibae, K. Ando, S. Maekawa and E. Saitoh, *Nature*, 2008, **455**, 778.
100 K. Uchida, J. Xiao, H. Adachi, J. Ohe, S. Takahashi, J. Ieda, T. Ota, Y. Kajiwara, H. Umezawa, H. Kawai, G. E. W. Bauer, S. Maekawa and E. Saitoh, *Nat. Mater.*, 2010, **9**, 894.
101 C. M. Jaworski, J. Yang, S. Mack, D. D. Awschalom, J. P. Heremans and R. C. Myers, *Nat. Mater.*, 2010, **9**, 898.
102 K. Uchidal, H. Adachi, T. Ota, H. Nakayama, S. Maekawa and E. Saitoh, *Appl. Phys. Lett.*, 2010, **97**, 172505.
103 A. Azevedo, S. Bharthulwar, W. R. Eppler and M. H. Kryder, *IEEE Trans. Magn.*, 1994, **30**, 4416.
104 T. Ishibashi, A. Mizusawa, M. Nagai, S. Shimizu, K. Sato, N. Togashi, T. Mogi, M. Houchido, H. Sano and K. Kuriyama, *J. Appl. Phys.*, 2005, **97**, 013516.
105 H. Lee, T. Kim, S. Kim, Y. Yoon, S. Kim, A. Babajan, T. Ishibashi, B. Friedman and K. Lee, *J. Magn. Magn. Mater.*, 2010, **322**, 2722.
106 J. Xiao, G. E. W. Bauer, K. Uchida, E. Saitoh and S. Maekawa, *Phys. Rev. B: Condens. Matter Mater. Phys.*, 2010, **81**, 214418.
107 H. Adachi, J. Ohe, S. Takahashi and S. Maekawa, *Phys. Rev. B: Condens. Matter Mater. Phys.*, 2011, **83**, 094410.
108 J.-S. Seo, J.-H. Jeon, Y. H. Hwang, H. Park, M. Ryu, S.-H. K. Park and B.-S. Bae, *Sci. Rep.*, 2013, **3**, 2085.
109 J. W. Jo, J. W. Jung, J. U. Lee and W. H. Jo, *ACS Nano*, 2010, **4**, 5382.
110 Q. Cao and J. A. Rogers, *Adv. Mater.*, 2009, **21**, 29.
111 K. K. Kim, S. M. Yoon, J. Y. Choi, J. Lee, B. K. Kim, J. M. Kim, J. H. Lee, U. Paik, M. H. Park, C. W. Yang, K. H. An, Y. S. Chung and Y. H. Lee, *Adv. Funct. Mater.*, 2007, **17**, 1775.
112 R. H. Schmidt, I. A. Kinloch, A. N. Burgess and A. H. Windle, *Langmuir*, 2007, **23**, 5707.
113 M. C. LeMieux, M. Roberts, S. Barman, Y. W. Jin, J. M. Kim and Z. N. Bao, *Science*, 2008, **321**, 101.
114 A. A. Green and M. C. Hersam, *Nano Lett.*, 2008, **8**, 1417.
115 M. Inagaki, Y. Yang and F. Kang, *Adv. Mater.*, 2012, **24**, 2547.
116 S. Cavaliere, S. Subianto, I. Savych, D. J. Jones and J. Roziere, *Energy Environ. Sci.*, 2011, **4**, 4761.
117 Y. M. Chen, Z. G. Lu, L. M. Zhou, Y. W. Mai and H. T. Huang, *Energy Environ. Sci.*, 2012, **5**, 7898.
118 A. Tsaroom, K. Matyjaszewski and M. S. Silverstein, *Polymer*, 2011, **52**, 2869.
119 E. Fortunato, D. Ginley, H. Hosono and D. C. Paine, *Mater. Res. Soc. Bull.*, 2007, **32**, 242.
120 D. J. Lipomi, M. Vosgueritchian, B. C. K. Tee, S. L. Hellstrom, J. A. Lee, C. H. Fox and Z. N. Bao, *Nat. Nanotechnol.*, 2011, **6**, 788.
121 H. L. Peng, W. H. Dang, J. Cao, Y. L. Chen, W. Wu, W. S. Zheng, H. Li, Z. X. Shen and Z. F. Liu, *Nat. Chem.*, 2012, **4**, 281.
122 A. Kumar and C. W. Zhou, *ACS Nano*, 2010, **4**, 11.
123 R. B. H. Tahar, T. Ban, Y. Ohya and Y. T. J. Takahashi, *Appl. Phys.*, 1998, **83**, 2631.
124 S. Kirchmeyer and K. J. Reuter, *J. Mater. Chem.*, 2005, **15**, 2077.
125 M. Zhang, S. L. Fang, A. A. Zakhidov, S. B. Lee, A. E. Aliev, C. D. Williams, K. R. Atkinson and R. H. Baughman, *Science*, 2005, **309**, 1215.
126 D. S. Hecht, L. B. Hu and G. Irvin, *Adv. Mater.*, 2011, **23**, 1482.
127 C. M. Niu, *Mater. Res. Soc. Bull.*, 2011, **36**, 766.
128 K. S. Kim, Y. Zhao, H. Jang, S. Y. Lee, J. M. Kim, K. S. Kim, J. H. Ahn, P. Kim, J. Y. Choi and B. H. Hee, *Nature*, 2009, **457**, 706.
129 F. Bonaccorso, Z. Sun, T. Hasan and A. C. Ferrari, *Nat. Photonics*, 2010, **4**, 611.
130 S. Bae, H. Kim, Y. Lee, X. F. Xu, J. S. Park, Y. Zheng, J. Balakrishnan, T. Lei, H. R. Kim, Y. Song, Y. J. Kim, K. S. Kim, B. Ozyilmaz, J. H. Ahn, B. H. Hong and S. Iijima, *Nat. Nanotechnol.*, 2010, **5**, 574.
131 D. S. Hecht and R. B. Kaner, *Mater. Res. Soc. Bull.*, 2011, **36**, 749.
132 S. De, M. H. Thomas, E. L. Philip, M. D. Evelyn, N. N. Peter, J. B. Werner, J. J. Boland and J. N. Coleman, *ACS Nano*, 2009, **3**, 1767.

133 E. C. Garnett, W. S. Cai, J. J. Cha, F. Mahmood, S. T. Connor, M. G. Christoforo, Y. Cui, M. D. McGehee and L. M. Brongersma, *Nat. Mater.*, 2012, **11**, 241.
134 L. B. Hu, H. Wu and Y. Cui, *Mater. Res. Soc. Bull.*, 2011, **36**, 760.
135 H. Wu, L. B. Hu, M. W. Rowell, D. S. Kong, J. J. Cha, J. R. McDonough, J. Zhu, Y. Yang, M. D. McGehee and Y. Cui, *Nano Lett.*, 2010, **10**, 4242.
136 M. G. Kang, M. S. Kim, J. S. Kim and L. J. Guo, *Adv. Mater.*, 2008, **20**, 4408.
137 J. V. Van de Groep, P. Spinelli and A. Polman, *Nano Lett.*, 2012, **12**, 3138.
138 D. S. Leem, A. Edwards, M. Faist, J. Nelson, D. D. C. Bradley and J. C. D. Mello, *Adv. Mater.*, 2011, **23**, 4371.
139 P. E. Lyons, S. De, J. Elias, M. Schamel, L. Philippe, A. T. Bellew, J. Boland and J. N. Coleman, *J. Phys. Chem. Lett.*, 2011, **2**, 3058.
140 H. Wu, D. Kong, Z. Ruan, P.-C. Hsu, S. Wang, Z. Yu, T. J. Carney, L. Hu, S. Fan and Y. Cui, *Nat. Nanotechnol.*, 2013, **8**, 421.
141 D. Li and Y. N. Xia, *Adv. Mater.*, 2004, **16**, 1151.
142 P. J. Kelly and R. D. Arnell, *Vacuum*, 2000, **56**, 159.
143 Y. Liang, D. Wu and R. Fu, *Sci. Rep.*, 2013, **3**, 1119.
144 D. Wu, F. Xu, B. Sun, R. Fu, H. He and K. Matyjaszewski, *Chem. Rev.*, 2012, **112**, 3959.
145 H. C. Bi, Z. Y. Yin, X. H. Cao, X. Xie, C. L. Tan, X. Huang, B. Chen, F. T. Chen, Q. L. Yang, X. Y. Bu, X. H. Lu, L. T. Sun and H. Zhang, *Adv. Mater.*, 2013, **25**, 5916.
146 M. F. El-Kady, V. Strong, S. Dubinand and R. B. Kaner, *Science*, 2012, **335**, 1326.
147 Y. Liang, D. Wu and R. Fu, *Langmuir*, 2009, **25**, 7783.
148 D. W. Wang, F. Li, M. Liu, G. Q. Lu and H. M. Cheng, *Angew. Chem., Int. Ed.*, 2008, **373**, 47.
149 X. Yang, D. Wu, X. Chen and R. J. Fu, *J. Phys. Chem. C*, 2010, **114**, 8581.
150 P. Simon and Y. Gogotsi, *Nat. Mater.*, 2008, **7**, 845.
151 F. Reincke, S. G. Hickey, W. K. Kegel and D. Vanmaekelbergh, *Angew. Chem., Int. Ed.*, 2004, **43**, 458.
152 L. Hu, M. Chen, X. Fang and L. Wu, *Chem. Soc. Rev.*, 2012, **41**, 1350.
153 Y. Ren, M. Chen, L. Hu, X. Fang and L. Wu, *J. Mater. Chem.*, 2012, **22**, 944.
154 Z. Niu, J. He, T. P. Russell and Q. Wang, *Angew. Chem., Int. Ed.*, 2010, **49**, 10052.
155 R. Ma, M. Osada, L. Hu and T. Sasaki, *Chem. Mater.*, 2010, **22**, 6341.
156 P. Pieranski, *Phys. Rev. Lett.*, 1980, **45**, 569.
157 Y. Lin, H. Skaff, T. Emrick, A. D. Dinsmore and T. P. Russell, *Science*, 2003, **299**, 226.
158 Y. Lin, H. Skaff, A. Böker, A. D. Dinsmore, T. Emrick and T. P. Russell, *J. Am. Chem. Soc.*, 2003, **125**, 12690.
159 Y. Lin, A. Böker, H. Skaff, D. Cookson, A. D. Dinsmore, T. Emrick and T. P. Russell, *Langmuir*, 2005, **21**, 191.
160 C. N. R. Rao and K. P. Kalyanikutty, *Acc. Chem. Res.*, 2008, **41**, 489.
161 I. Benjamin, *Chem. Rev.*, 1996, **96**, 1449.
162 M. K. Jana, P. Chithaiah, B. Murali, S. B. Krupanidhi, K. Biswas and C. N. R. Rao, *J. Mater. Chem. C*, 2013, **1**, 6184.
163 C. N. R. Rao, G. U. Kulkarni, P. J. Thomas, V. V. Agrawal and P. Saravanan, *J. Phys. Chem. B*, 2003, **107**, 7391.
164 V. V. Agrawal, G. U. Kulkarni and C. N. R. Rao, *J. Phys. Chem. B*, 2005, **109**, 7300.
165 M. K. Sanyal, V. V. Agrawal, M. K. Bera, K. P. Kalyanikutty, J. Daillant, C. Blot, S. Kubowicz, O. Konovalov and C. N. R. Rao, *J. Phys. Chem. C*, 2008, **112**, 1739.
166 V. V. Agrawal, G. U. Kulkarni and C. N. R. Rao, *J. Colloid Interface Sci.*, 2008, **318**, 501.
167 V. V. Agrawal, N. Varghese, G. U. Kulkarni and C. N. R. Rao, *Langmuir*, 2008, **24**, 2495.
168 R. Krishnaswamy, S. Majumdar, R. Ganapathy, V. V. Agrawal, A. K. Sood and C. N. R. Rao, *Langmuir*, 2007, **23**, 3084.
169 V. V. Agrawal, P. Mahalakshmi, G. U. Kulkarni and C. N. R. Rao, *Langmuir*, 2006, **22**, 1846.
170 C. N. R. Rao, G. U. Kulkarni, V. V. Agrawal, U. K. Gautam, M. Ghosh and U. Tumkurkar, *J. Colloid Interface Sci.*, 2005, **289**, 305.
171 U. K. Gautam, M. Ghosh and C. N. R. Rao, *Chem. Phys. Lett.*, 2003, **381**, 1.
172 U. K. Gautam, M. Ghosh and C. N. R. Rao, *Langmuir*, 2004, **20**, 10775.
173 K. P. Kalyanikutty, U. K. Gautam and C. N. R. Rao, *Solid State Sci.*, 2006, **8**, 296.
174 K. P. Kalyanikutty, U. K. Gautam and C. N. R. Rao, *J. Nanosci. Nanotechnol.*, 2007, **7**, 1916.
175 S. Keuleyan, E. Lhuillier, V. Brajuskovic and P. G. Sionnest, *Nat. Photonics*, 2011, **5**, 489.
176 J. Ge and Y. Yin, *Angew. Chem., Int. Ed.*, 2011, **50**, 1492.
177 J. G. McGrath, R. D. Bock, J. M. Cathcart and L. A. Lyon, *Chem. Mater.*, 2007, **19**, 1584.
178 H. Kim, J. Ge, J. Kim, S.-e. Choi, H. Lee, H. Lee, W. Park, Y. Yin and S. Kwon, *Nat. Photonics*, 2009, **3**, 534.
179 K. Matsubara, M. Watanabe and Y. Takeoka, *Angew. Chem.*, 2007, **119**, 1718; K. Matsubara, M. Watanabe and Y. Takeoka, *Angew. Chem., Int. Ed.*, 2007, **46**, 1688.
180 C. Schliehe, B. H. Juarez, M. Pelletier, S. Jander, D. Greshnykh, M. Nagel, A. Meyer, S. Foerster, A. Kornowski, C. Klinke and H. Weller, *Science*, 2010, **329**, 550.
181 X. Zhang, J. Zhang, J. Zhao, B. Pan, M. Kong, J. Chen and Y. Xie, *J. Am. Chem. Soc.*, 2012, **134**, 11908.
182 T. Yu, B. Lim and Y. Xia, *Angew. Chem., Int. Ed.*, 2010, **49**, 4484.
183 L. Li, Z. Chen, Y. Hu, X. Wang, T. Zhang, W. Chen and Q. Wang, *J. Am. Chem. Soc.*, 2013, **135**, 1213.
184 C. Wu, F. Feng and Y. Xie, *Chem. Soc. Rev.*, 2013, **42**, 5157.
185 M. Guan, C. Xiao, J. Zhang, S. Fan, R. An, Q. Cheng, J. Xie, M. Zhou, B. Ye and Y. Xie, *J. Am. Chem. Soc.*, 2013, **135**, 10411.
186 X. Zhang and Y. Xie, *Chem. Soc. Rev.*, 2013, **42**, 8187.
187 S. Z. Butler, S. M. Hollen, L. Cao, Y. Cui, J. A. Gupta, H. R. Gutierrez, T. F. Heinz, S. S. Hong, J. Huang, A. F. Ismach, E. Johnston-Halperin, M. Kuno, V. V. Plashnitsa,

R. D. Robinson, R. S. Ruoff, S. Salahuddin, J. Shan, L. Shi, M. G. Spencer, M. Terrones, W. Windl and J. E. Goldberger, *ACS Nano*, 2013, **7**, 2898.
188 K. S. Novoselov, A. K. Geim, S. V. Morozov, D. Jiang, Y. Zhang, S. V. Dubonos, I. V. Grigorieva and A. A. Firsov, *Nature*, 2004, **306**, 666.
189 R. Ma and T. Sasaki, *Adv. Mater.*, 2010, **22**, 5082.
190 J. N. Coleman, M. Lotya, A. O'Neill, S. D. Bergin, P. J. King, U. Khan, K. Young, A. Gaucher, S. De, R. J. Smith, I. V. Shvets, S. K. Arora, G. Stanton, H. Y. Kim, K. Lee, G. T. Kim, G. S. Duesberg, T. Hallam, J. J. Boland, J. J. Wang, J. F. Donegan, J. C. Grunlan, G. Moriarty, G. Moriarty, A. Shmeliov, R. J. Nicholls, J. M. Perkins, E. M. Grieveson, K. Theuwissen, D. W. McComb, P. D. Nellist and V. Nicolosi, *Science*, 2011, **331**, 568.
191 Z. Y. Zeng, Z. Y. Yin, X. Huang, H. Li, Q. Y. He, G. Lu, F. Boey and H. Zhang, *Angew. Chem., Int. Ed.*, 2011, **50**, 11093.
192 Y. Sun, Z. Sun, S. Gao, H. Cheng, Q. Liu, J. Piao, T. Yao, C. Wu, S. Hu, S. Wei and Y. Xie, *Nat. Commun.*, 2012, **3**, 1057.
193 Q. Wang and D. O'Hare, *Chem. Rev.*, 2012, **112**, 4124.
194 D. P. Yan, J. Lu, M. Wei, J. Ma, D. G. Evans and X. Duan, *AIChE J.*, 2011, **57**, 1926.
195 T. Sasaki, S. Nakano, S. Yamauchi and M. Watanabe, *Chem. Mater.*, 1997, **9**, 602.
196 X. Wang, Y. Zhong, T. Zhai, Y. Guo, S. Chen, Y. Ma, J. Yao, Y. Bando and D. Golberg, *J. Mater. Chem.*, 2011, **21**, 17680.
197 D. Liu, X. Wang, X. Wang, W. Tian, J. Liu, C. Zhi, D. He, Y. Bando and D. Golberg, *J. Mater. Chem. A*, 2013, **1**, 1952.
198 X. Wang, W. Tian, T. Zhai, C. Zhi, Y. Bando and D. Golberg, *J. Mater. Chem.*, 2012, **22**, 23310.
199 C. Nethravathi, C. R. Rajamathi, M. Rajamathi, U. K. Gautam, X. Wang, D. Golberg and Y. Bando, *ACS Appl. Mater. Interfaces*, 2013, **5**, 2708.
200 M. Zhang, T. Zhai, X. Wang, Y. Ma and J. Yao, *Cryst. Growth Des.*, 2010, **10**, 1201.
201 X. Yang, C. Cheng, Y. Wang, L. Qiu and D. Li, *Science*, 2013, **341**, 534.
202 X. Lang, A. Hirata, T. Fujita and M. Chen, *Nat. Nanotechnol.*, 2011, **6**, 232.
203 T. Fujital, H. Okada, K. Koyama, K. Watanabe, S. Maekawa and M. W. Chen, *Phys. Rev. Lett.*, 2008, **101**, 166601.
204 J. Erlebacher, M. J. Aziz, A. Karma, N. Dimitrov and K. Sieradzki, *Nature*, 2001, **410**, 450.
205 H. Guan, X. Wang, H. Li, C. Zhi, T. Zhai, Y. Bando and D. Golberg, *Chem. Commun.*, 2012, **48**, 4878.
206 H. Guan, X. Wang, S. Chen, Y. Bando and D. Golberg, *Chem. Commun.*, 2011, **47**, 12098.
207 B. Liu, Z. R. Wang, Y. Dong, Y. G. Zhu, Y. Gong, S. H. Ran, Z. Liu, J. Xu, Z. Xie, D. Chen and G. Z. Shen, *J. Mater. Chem.*, 2012, **22**, 9379.
208 Y. Z. Jin, J. P. Wang, B. Q. Sun, J. C. Blakesley and N. C. Greenham, *Nano Lett.*, 2008, **8**, 1649.
209 D. L. Shao, M. P. Yu, H. T. Sun, T. Hu, J. Lian and S. Sawyer, *Nanoscale*, 2013, **5**, 3664.
210 G. Konstantatos, L. Levina, J. Tang and E. H. Sargent, *Nano Lett.*, 2008, **8**, 4002.
211 G. Konstantatos, I. Howard, A. Fischer, S. Hoogland, J. Clifford, E. Klem, L. Levina and E. H. Sargent, *Nature*, 2006, **442**, 180.
212 J. J. Wang, Y. Q. Wang, F. F. Cao, Y. G. Guo and L. J. Wan, *J. Am. Chem. Soc.*, 2010, **132**, 12218.
213 P. J. Li, Z. M. Liao, X. Z. Zhang, X. J. Zhang, H. C. Zhu, J. Y. Gao, K. Laurent, Y. L. Wang, N. Wang and D. P. Yu, *Nano Lett.*, 2009, **9**, 2513.
214 S. E. Ahn, J. S. Lee, H. Kim, S. Kim, B. H. Kang, K. H. Kim and G. T. Kim, *Appl. Phys. Lett.*, 2004, **84**, 5022.
215 P. Gao, Z. Z. Wang, K. H. Liu, Z. Xu, W. L. Wang, X. D. Bai and E. G. Wang, *J. Mater. Chem.*, 2009, **19**, 1002.
216 B. Aksoy, S. Coskun, S. Kucukyildiz and H. E. Unalan, *Nanotechnology*, 2012, **23**, 325202.
217 A. Rostami, M. Dolatyari, E. Amini, H. Rasooli, H. Baghban and S. Miri, *ChemPhysChem*, 2013, **14**, 554.
218 H. X. Chang, Z. H. Sun, K. Y. F. Ho, X. M. Tao, F. Yan, W. M. Kwok and Z. J. Zheng, *Nanoscale*, 2011, **3**, 258.
219 H. Kind, H. Q. Yan, B. Messer, M. Law and P. D. Yang, *Adv. Mater.*, 2002, **14**, 158.
220 B. Chitara, L. S. Panchakarla, S. B. Krupanidhi and C. N. R. Rao, *Adv. Mater.*, 2011, **23**, 5419.
221 B. Chitara, S. B. Krupanidhi and C. N. R. Rao, *Appl. Phys. Lett.*, 2011, **99**, 113114.
222 P. A. Hu, L. F. Wang, M. Yoon, J. Zhang, W. Feng, X. N. Wang, Z. Z. Wen, J. C. Idrobo, Y. Miyamoto, D. B. Geohegan and K. Xiao, *Nano Lett.*, 2013, **13**, 1649.
223 F. N. Xia, T. Mueller, Y. M. Lin, A. Valades- Garcia and P. Avouris, *Nat. Nanotechnol.*, 2009, **4**, 839.
224 K. K. Manga, J. Z. Wang, M. Lin, J. Zhang, M. Nesladek, V. Nalla, W. Ji and K. P. Loh, *Adv. Mater.*, 2012, **24**, 1697.
225 G. Konstantatos, M. Badioli, L. Gaudreau, J. Osmond, M. Bernechea, F. P. G. de Arquer, F. Gatti and F. H. L. Koppens, *Nat. Nanotechnol.*, 2012, **7**, 363.
226 L. S. Li, R. G. Cao, Z. J. Wang, J. J. Li and L. M. Qi, *J. Phys. Chem. C*, 2009, **113**, 18075.
227 W. Z. Shan, L. F. Hu, X. Lin, M. Chen and L. M. Wu, *J. Mater. Chem.*, 2012, **22**, 17671.
228 D. Liu, X. Wang, X. Wang, W. Tian, Y. Bando and D. Golberg, *Sci. Rep.*, 2013, **3**, 2543.
229 C. Yan, N. Singh and P. S. Lee, *Appl. Phys. Lett.*, 2010, **96**, 053108.
230 K. Liu, M. Sakurai, M. Y. Liao and M. Aono, *J. Phys. Chem. C*, 2010, **114**, 19835.

